

Black holes and fundamental fields in Numerical Relativity: initial data construction and evolution of bound states

Hirotsada Okawa,^{1,*} Helvi Witek,^{2,†} and Vitor Cardoso^{1,3,4,‡}

¹*CENTRA, Departamento de Física, Instituto Superior Técnico,
Universidade Técnica de Lisboa - UTL, Avenida Rovisco Pais 1, 1049 Lisboa, Portugal.*

²*Department of Applied Mathematics and Theoretical Physics, Centre for Mathematical Sciences,
University of Cambridge, Wilberforce Road, Cambridge CB3 0WA, UK*

³*Perimeter Institute for Theoretical Physics, Waterloo, Ontario N2L 2Y5, Canada.*

⁴*Department of Physics and Astronomy, The University of Mississippi, University, MS 38677, USA.*

(Dated: March 24, 2014)

Fundamental fields are a natural outcome in cosmology and particle physics and might therefore serve as a proxy for more complex interactions. The equivalence principle implies that all forms of matter gravitate, and one therefore expects relevant, universal imprints of new physics in strong field gravity, such as that encountered close to black holes. Fundamental fields in the vicinities of supermassive black holes give rise to extremely long-lived, or even unstable, configurations which slowly extract angular momentum from the black hole or simply evolve non-linearly over long timescales, with important implications for particle physics and gravitational-wave physics.

Here, we perform a fully non-linear study of scalar-field condensates around rotating black holes. We provide novel ways to specify initial data for the Einstein-Klein-Gordon system, with potential applications in a variety of scenarios. Our numerical results confirm the existence of long-lived bar-modes which act as lighthouses for gravitational wave emission: the scalar field condenses outside the black hole geometry and acts as a constant frequency gravitational-wave source for very long timescales. This effect could turn out to be a potential signature of beyond standard model physics and also a promising source of gravitational waves for future gravitational wave detectors.

PACS numbers: 98.80.Es, 04.30.-w, 11.25.Wx, 14.80.Va, 04.70.-s

I. INTRODUCTION

Black holes (BHs) are among the most fascinating and numerous inhabitants of our universe, a remarkable consequence of General Relativity (GR) or extensions thereof. Stellar mass BHs of a few solar masses ($3M_\odot \lesssim M_{\text{BH}} \lesssim 30M_\odot$) are expected to be the end-state of massive stars; compelling evidence for their existence is provided by observations of ultra-compact binaries made up of pulsars and BHs as well as observations of BHs accreting matter from surrounding disks [1–8]. On the other end of the mass spectrum we expect supermassive BHs (SMBHs) with $10^6 M_\odot \lesssim M_{\text{BH}} \lesssim 10^9 M_\odot$ to be hosted at the centre of most galaxies and, in fact, observations of trajectories of stars close to the centre of the Milky Way hint at “our very own” SMBH with mass $M_{\text{BH}} \sim 4.2 \cdot 10^6 M_\odot$ [9–17]. Many of the aforementioned observations ranging from the radio to the X-ray frequency band allow for accurate estimates of the mass and spin of these BHs, thus making precision BH physics possible; this in turn may allow a mapping of compact objects across the visible universe with second generation ground-based gravitational wave (GW) observatories such as the advanced LIGO / VIRGO network [18–23], the KAGRA detector [24, 25] currently under construc-

tion or future space-based LISA-like missions [7, 26].

Fundamental fields – either constituents of dark matter or other types of stable fundamental fields – may play a crucial role in the context of GW emission and detection. They may influence how a SMBH is bound to its host galaxy or affect the very properties of both stellar-mass or supermassive BH systems and, consequently, their GW emission [27–29]. One example of such drastic effects concerns the existence of very long lived massive states of fundamental fields around BHs and their possible growth via superradiance [30–32]. We remind the reader that (rotational-induced) superradiance of a wavepacket of (real) frequency ω_R requires the condition

$$0 < \omega_R < m\Omega_H = \omega_C, \quad (1)$$

where m is an azimuthal number and Ω_H is the BH’s angular frequency. This mechanism to amplify waves scattering off Kerr BHs allows for exciting phenomena: one example is the Gedankenexperiment suggested in Refs. [30, 31, 33], and consists of enclosing the system by a perfectly reflecting mirror. The bouncing on the mirror and amplification in the ergoregion will result in an exponential growth of the field and an increasing “radiation” pressure will eventually render the system unstable. This so-called “black-hole bomb” mechanism [33] or “superradiant instability” has attracted some attention over the years [30, 31, 33–38].

Astrophysical “BH bombs” may exist in the presence of ultralight degrees of freedom, thought to arise in a va-

* hirotada.okawa@ist.utl.pt

† h.witek@damtp.cam.ac.uk

‡ vitor.cardoso@ist.utl.pt

riety of scenarios [29, 39, 40]¹. Massive fields in general can create a “trapping well” some distance away from the BH, with a tail that extends into the ergoregion, effectively working as a confining box at low frequencies [45–47]. An exploration of the behavior of massive fields in the vicinities of BHs has uncovered remarkable results, ranging from floating orbits to the possibility of constraining fundamental fields from the observation of SMBHs [48, 49]. This has led to a vast number of investigations of massive fields around rotating BHs in the frequency- [48–54] and in the time-domain [38, 55–58].

These incursions are also motivated by extensions of General Relativity such as scalar-tensor theories [59–62] but also by the “axiverse” scenario proposed in Refs. [29, 40, 63]. Inspired by the QCD axion [39] Arvanitaki et al [29, 40] suggested the existence of a plethora of ultra-light bosonic degrees of freedom which could play an important role in BH astrophysics if their masses range from $10^{-21}\text{eV} \lesssim \mu_S \lesssim 10^{-8}\text{eV}$. Conversely, the observation of BHs in a certain mass–spin parameter range can put stringent constraints on the existence of these particles as suggested in Refs. [29, 64]. In other words, one can use SMBHs to explore beyond-standard model physics.

Within the past year, these studies inspired a “gold-rush” of investigations going beyond the simplest model considering scalar fields in GR [49, 57, 58, 64–75] (see also, e.g., Refs. [76, 77] for recent reviews). Recently, it was shown that the superradiant instability can, at least for complex scalars, drive the system to a new, truly stationary solution describing a hairy BH [78].

Despite this immense progress in exploring the superradiant mechanism in various configurations most dynamical studies so far have been restricted to the *linearized* regime, i.e. fixing the BH spacetime as a background over which matter fields evolve (but see Ref. [32] for recent fully non-linear investigations). While this assumption is valid as long as the amplified field is small, it is inevitable to break down eventually. Then, back-reaction onto the spacetime will become important. Depending on the frequency composition of the field this might yield spin-down and mass-loss of the central BH in the superradiant regime or accretion, i.e., increase of the BH spin and mass in the “normal” regime.

Thus, the question about the end-state of the instability remains; both scenarios, that of a true non-linear instability as well as a quasi-equilibrium configuration, might be possible. In fact, this is exactly the regime with potentially exciting new physical signatures: The formation of a bosonic cloud around BHs

might produce a “gravitational atom”, where the name is adopted due to the hydrogen-like spectrum of the field [49, 51], possibly observable through scalar and (modified) GW emission. Depending on the efficiency with which the bosonic cloud can be accreted, we might even observe GW pulsars or “light-houses” or find gaps in the Regge plane, i.e., the mass-spin phase-space of BHs [29, 40, 48, 63, 64, 76, 77, 79, 80]. The evolution may also drive the system to a new stationary state such as the hairy BH solutions recently uncovered [78], although these solutions are also likely to be unstable, at least in part of the solution parameter space [81]. The understanding of all these possibilities require nonlinear evolutions of the equations of motion.

In the present study we explore the effects of the back-reaction and nonlinearities of the field equations by performing full-blown numerical simulations of GR coupled to a minimally coupled massive scalar field.

As guideline for our investigations let us briefly review the key results of linearized studies concerning massive scalar fields surrounding Kerr BHs [38, 48–53, 57, 58]. First of all, because of the presence of the potential well due to the mass term, two types of modes are possible – quasi-normal modes (QNMs) which decay at infinity and quasi-bound state modes (BSMs) which are localized in the dip of the potential around the BH. The latter class can yield exponentially growing modes if the BH is spinning. Because these are dynamical, non-stationary spacetimes, the no-hair theorem is *not* violated. The strongest instability growth rate of $\omega_I \equiv \frac{1}{\tau} \sim 1.5 \cdot 10^{-7} \left(\frac{GM}{c^3}\right)^{-1}$ was found for the $l = m = 1$ mode of a massive scalar with mass coupling $M_{\text{BH}}\mu = 0.42$ evolving around a rotating BH with spin $a/M_{\text{BH}} = 0.99$ [50, 51]. Here τ is the typical instability timescale. Recent simulations in the time domain [38, 57, 58] revealed beating phenomena for generic Gaussian wave packets due to the presence of various overtone modes and space dependent excitation of modes; very much like the excitation and modulation of tones as a guitar string is excited. The latter effect has been further investigated in Ref. [82]. Guided by these results, we will numerically evolve complex, massive scalar fields initialized both as generic Gaussian pulse as well as pseudo-bound states with a mass coupling close to the one expected for strong instability growth rates around Kerr BHs. Following the approach in Liu et al [83] we have been able to accurately set up puncture initial data representing Kerr BHs with an initial spin up to 95% of the Kerr bound.

This paper is organized as follows: In Sec. II we will describe the setup of our model and its formulation as Cauchy problem. We complement the setup by constructing constraint-preserving initial data in Sec. III. In particular, we develop analytic and numerical solutions for a number of different configurations involving Schwarzschild or Kerr BHs surrounded by “scalar clouds”. In Secs. IV–V we present the results of our non-linear time evolutions starting, respectively, with non-rotating or highly rotating BHs. We finalize the paper

¹ A very natural “BH bomb” also arises in asymptotically anti-de Sitter (AdS) spacetimes, for which the timelike boundary takes on the role of the reflecting cavity. Indeed, it has been shown that small Kerr-AdS BHs do suffer from the superradiant instability [34, 41–44]. Although they are not relevant for astrophysical scenarios, BHs in AdS play an important role in high energy physics, in particular in the context of the gauge/gravity duality.

with some conclusions and prospects for future work in Sec. VI. Further checks of our numerical simulations including error estimates and benchmark tests can be found in Appendices A and B. Finally, illustrative snapshots of the evolution are shown in Appendix C. Unless stated otherwise we work in natural units, i.e., $G = 1 = c$.

II. SETUP

We wish to explore the non-linear dynamics of scalar clouds in the environment of rotating BHs. This system is modelled by the Einstein–Hilbert action (in 4-dimensional asymptotically flat spacetimes) minimally coupled to a complex, massive scalar field Φ with mass parameter $\mu_S = m_S/\hbar$ and described by the action [84, 85]

$$S = \int d^4x \sqrt{-g} \left(\frac{{}^{(4)}R}{16\pi} + \mathcal{L}_\Phi \right), \quad \text{with} \quad (2a)$$

$$\mathcal{L}_\Phi = -\frac{1}{2}g^{\mu\nu}\partial_\mu\Phi^*\partial_\nu\Phi - \frac{1}{2}\mu_S^2\Phi^*\Phi - V(\Phi), \quad (2b)$$

where ${}^{(4)}R$ is the 4-dimensional Ricci scalar and $V(\Phi)$ is the scalar field potential. The variation of the action (2) with respect to the metric and scalar field yields, respectively, the tensor and scalar equations of motion (EoMs)

$${}^{(4)}R_{\mu\nu} - \frac{1}{2}g_{\mu\nu} {}^{(4)}R - 8\pi T_{\mu\nu} = 0, \quad (3a)$$

$$(\nabla^\mu \nabla_\mu - \mu_S^2)\Phi - V'(\Phi) = 0, \quad (3b)$$

where the energy-momentum tensor of the scalar field is determined by

$$T_{\mu\nu} = -\frac{1}{2}g_{\mu\nu}(\partial_\lambda\Phi^*\partial^\lambda\Phi + \mu_S^2\Phi^*\Phi) - g_{\mu\nu}V(\Phi) + \frac{1}{2}(\partial_\mu\Phi^*\partial_\nu\Phi + \partial_\mu\Phi\partial_\nu\Phi^*). \quad (4)$$

Time evolution formulation: Because we intend to explore the non-linear GR-scalar field system in the highly dynamical, strong curvature regime we need to solve the EoMs (3) numerically. Therefore, we employ standard Numerical Relativity (NR) techniques [86–92] based on the 3+1 decomposition. Within this approach the 4-dimensional spacetime manifold $(\mathcal{M}, g_{\mu\nu})$ is foliated into 3-dimensional spatial hypersurfaces (Σ_t, γ_{ij}) which are parametrized by the time coordinate t . The spatial metric γ_{ij} is related to the spacetime metric $g_{\mu\nu}$ via $\gamma_{\mu\nu} = g_{\mu\nu} + n_\mu n_\nu$ and n^μ is the unit vector normal to the hypersurfaces. The spacetime line element writes

$$ds^2 = g_{\mu\nu}dx^\mu dx^\nu = -(\alpha^2 - \beta_i\beta^i)dt^2 + 2\gamma_{ij}\beta^i dt dx^j + \gamma_{ij}dx^i dx^j, \quad (5)$$

where the lapse function α and shift vector β^i encode the coordinate degrees of freedom. We proceed by casting Eqs. (3) into a Cauchy problem such that they are “digestible” by computers. In a nutshell, we rewrite them

as a time evolution problem with constraints along the lines of the ADM–York decomposition [88, 93]. To this end, we introduce the conjugated momenta to the scalar field, Π , and to the metric, K_{ij} . The extrinsic curvature K_{ij} describes how the spatial hypersurfaces are embedded into the full spacetime. These quantities are defined by,

$$K_{ij} = -\frac{1}{2\alpha}(\partial_t - \mathcal{L}_\beta)\gamma_{ij}, \quad \Pi = -\frac{1}{\alpha}(\partial_t - \mathcal{L}_\beta)\Phi. \quad (6)$$

Here, \mathcal{L}_β denotes the Lie derivative along the shift vector β^i . The definitions (6) immediately provide a prescription for the time evolution of the 3-metric and scalar field

$$(\partial_t - \mathcal{L}_\beta)\gamma_{ij} = -2\alpha K_{ij}, \quad (\partial_t - \mathcal{L}_\beta)\Phi = -\alpha\Pi, \quad (7)$$

capturing the kinematical degrees of freedom. Performing the 3+1 decomposition of Eqs. (3) yields the Hamiltonian and momentum constraints

$$\mathcal{H} = R + K^2 - K_{ij}K^{ij} - 16\pi\rho = 0, \quad (8a)$$

$$\mathcal{M}_i = D_j K^j_i - D_i K - 8\pi j_i = 0, \quad (8b)$$

as well as time evolution equations for the extrinsic curvature and scalar field momentum

$$(\partial_t - \mathcal{L}_\beta)K_{ij} = -D_i D_j \alpha + \alpha(R_{ij} - 2K^k_i K_{jk} + K K_{ij}) + 4\pi\alpha(\gamma_{ij}(S - \rho) - 2S_{ij}), \quad (9a)$$

$$(\partial_t - \mathcal{L}_\beta)\Pi = \alpha(-D^i D_i \Phi + K\Pi + \mu_S^2\Phi + V'(\Phi)) - D^i \alpha D_i \Phi, \quad (9b)$$

where R_{ij} and R refer to the 3-dimensional Ricci tensor and scalar associated with the spatial metric γ_{ij} . The energy density ρ , energy-momentum flux j_i and spatial components S_{ij} of the energy momentum tensor (4) are given by

$$\rho = \frac{1}{2}\Pi^*\Pi + \frac{1}{2}\mu_S^2\Phi^*\Phi + \frac{1}{2}D^i\Phi^*D_i\Phi + V(\Phi), \quad (10a)$$

$$j_i = \frac{1}{2}(\Pi^*D_i\Phi + \Pi D_i\Phi^*), \quad (10b)$$

$$S_{ij} = \frac{1}{2}(D_i\Phi^*D_j\Phi + D_i\Phi D_j\Phi^*) - \gamma_{ij}V(\Phi) + \frac{1}{2}\gamma_{ij}(\Pi^*\Pi - \mu_S^2\Phi^*\Phi - D^k\Phi^*D_k\Phi). \quad (10c)$$

We now have all necessary ingredients at hand to simulate scalar fields in GR. Unfortunately, the evolution equations (7) and (9) are known to pose only a weakly hyperbolic set of PDEs [86, 94, 95] and are, thus, prone to numerical instabilities.

BSSN formulation: In order to circumvent the ill-posedness of Eqs. (7) and (9) and to obtain a stable numerical formulation we need to modify the evolution PDEs. Specifically, we employ the strongly hyperbolic, well-posed scheme introduced by Baumgarte & Shapiro [96] and Shibata & Nakamura [97] (BSSN). The key idea is to add the constraints (8) to the ADM–York like Eqs. (7) and (9) in a specific manner, thus changing the character of the PDEs. Additionally, it has been

found convenient to introduce a set of conformal variables as dynamical quantities. The BSSN variables are given by

$$\chi = \gamma^{-\frac{1}{3}}, \quad \tilde{\gamma}_{ij} = \gamma^{-\frac{1}{3}} \gamma_{ij} = \chi \gamma_{ij}, \quad (11a)$$

$$K = \gamma^{ij} K_{ij}, \quad \tilde{A}_{ij} = \chi A_{ij} = \chi (K_{ij} - \frac{1}{3} \gamma_{ij} K), \quad (11b)$$

$$\tilde{\Gamma}^i = \tilde{\gamma}^{jk} \tilde{\Gamma}^i_{jk} = -\partial_j \tilde{\gamma}^{ij}, \quad (11c)$$

where χ and $\tilde{\gamma}_{ij}$ are the conformal factor and metric, K and \tilde{A}_{ij} are the trace and conformal tracefree part of the extrinsic curvature and $\tilde{\Gamma}^i$ is the conformal connection function. We denote $\gamma = \det \gamma_{ij}$, while $\tilde{\gamma} = \det \tilde{\gamma}_{ij} = 1$ holds by construction. We will not discuss the derivation of the BSSN equations and instead only present the final expressions for a vanishing scalar field potential $V(\Phi) = 0$

$$\partial_t \chi = [\text{BSSN}], \quad (12a)$$

$$\partial_t \tilde{\gamma}_{ij} = [\text{BSSN}], \quad (12b)$$

$$\partial_t K = [\text{BSSN}] + 8\pi\alpha \left(\Pi^* \Pi - \frac{\mu_S^2}{2} \Phi^* \Phi \right), \quad (12c)$$

$$\partial_t \tilde{A}_{ij} = [\text{BSSN}] - 4\pi\alpha\chi \left(\tilde{D}_i \Phi^* \tilde{D}_j \Phi + \tilde{D}_i \Phi \tilde{D}_j \Phi^* - \frac{2}{3} \tilde{\gamma}_{ij} \tilde{D}^k \Phi^* \tilde{D}_k \Phi \right), \quad (12d)$$

$$\partial_t \tilde{\Gamma}^i = [\text{BSSN}] - 8\pi\alpha \tilde{\gamma}^{ij} \left(\Pi^* \tilde{D}_j \Phi + \Pi \tilde{D}_j \Phi^* \right), \quad (12e)$$

$$\partial_t \Phi = -\alpha \Pi + \mathcal{L}_\beta \Phi, \quad (12f)$$

$$\begin{aligned} \partial_t \Pi = & \alpha \left(-\chi \tilde{D}^i \tilde{D}_i \Phi + \frac{1}{2} \tilde{D}^i \Phi \tilde{D}_i \chi + K \Pi + \mu_S^2 \Phi \right) \\ & - \chi \tilde{D}^i \alpha \tilde{D}_i \Phi + \mathcal{L}_\beta \Pi, \end{aligned} \quad (12g)$$

where “[BSSN]” denotes the vacuum BSSN equations given, e.g., in Refs. [86, 87, 89–92, 98] and \tilde{D}_i is the covariant derivative with respect to the conformal metric $\tilde{\gamma}_{ij}$.

In order to close the PDE system (12) we additionally have to specify the coordinates. In particular, we choose the moving puncture gauge [86, 87, 99–101], i.e., the $1 + \log$ -slicing for the lapse function α and the Γ -driver shift condition for β^i

$$\partial_t \alpha = \beta^k \partial_k \alpha - 2\alpha K, \quad (13a)$$

$$\partial_t \beta^i = \beta^k \partial_k \beta^i - \eta_\beta \beta^i + \zeta_\Gamma \tilde{\Gamma}^i. \quad (13b)$$

This system of equations was supplemented with Sommerfeld boundary conditions far away. To ensure that the boundary conditions are not contaminating our results, the outer boundary of the numerical domain is placed sufficiently far away as to be causally disconnected from the region under study, and each of the simulations we discuss was stopped before spurious reflections from the outer boundary can contaminate the results. We have verified *a posteriori* that the grid size is also larger than any characteristic wavelength showing up in our results. Our results are convergent and stable when the grid size is varied.

Extraction of physical information: Finally, we give a brief summary of the tools that we will employ to analyze our numerical data. These include in particular (i) the extraction of scalar and GWs, (ii) the computation of the energy radiated in these signals, and (iii) the estimation of the BH mass and spin using information about the apparent horizon (AH). An extended discussion of either method can be found, e.g., in Refs. [37, 86, 87] and references therein.

As a measure for the scalar and gravitational radiation we extract the scalar field Φ and the Newman-Penrose scalar Ψ_4 , which encodes the outgoing gravitational radiation [102, 103], at coordinate spheres of fixed radius r_{ex} . Because we are interested in the multipolar structure of the radiated signals we project $\Phi(t, r = r_{\text{ex}}, \theta, \varphi)$ and $\Psi_4(t, r = r_{\text{ex}}, \theta, \varphi)$ with, respectively, spherical and $s = -2$ spin-weighted spherical harmonics

$$\Phi_{lm}(t, r_{\text{ex}}) = \int d\Omega \Phi(t, r_{\text{ex}}, \theta, \varphi) Y^*_{lm}(\theta, \varphi), \quad (14)$$

$$\Psi_{4,lm}(t, r_{\text{ex}}) = \int d\Omega \Psi_4(t, r_{\text{ex}}, \theta, \varphi) {}_{-2}Y^*_{lm}(\theta, \varphi).$$

We estimate the radiated energy and angular momentum content in the GWs Ψ_4 by (see Eqs. (22)–(24) in Ref. [37] and references therein)

$$\frac{dE}{dt} = \lim_{r \rightarrow \infty} \frac{r^2}{16\pi} \int d\Omega \left| \int_{-\infty}^t \Psi_4 d\tilde{t} \right|^2, \quad (15a)$$

$$\frac{dP_i}{dt} = - \lim_{r \rightarrow \infty} \frac{r^2}{16\pi} \int d\Omega \ell_i \left| \int_{-\infty}^t \Psi_4 d\tilde{t} \right|^2, \quad (15b)$$

$$\begin{aligned} \frac{dJ_z}{dt} = & - \lim_{r \rightarrow \infty} \frac{r^2}{16\pi} \times \Re \left[\int d\Omega \left(\int_{-\infty}^t \Psi_4 d\tilde{t} \right) \right. \\ & \left. \partial_\varphi \left(\int_{-\infty}^t \int_{-\infty}^{\tilde{t}} \Psi^*_{-4} d\tilde{t} d\tilde{t} \right) \right], \end{aligned} \quad (15c)$$

with $\ell = (-\sin \theta \cos \varphi, -\sin \theta \sin \varphi, -\cos \theta)$. In order to access the properties and evolution of the BH itself we characterize its AH (by using for example the AHFINDERDIRECT [104, 105]), in terms of its area A_{AH} , equatorial circumference C_e , and irreducible mass $M_{\text{irr}} = \sqrt{A_{\text{AH}}/(16\pi)}$, among other data. We use this information to compute the BH dimensionless spin

$$j_{\text{AH}} \equiv \frac{J}{M_{\text{BH}}^2} = \sqrt{1 - \left(\frac{2\pi A_{\text{AH}}}{C_e^2} - 1 \right)^2}, \quad (16)$$

and mass according to Christodoulou’s formula [106]

$$M_{\text{BH}}^2 = M_{\text{irr}}^2 + \frac{J^2}{4M_{\text{irr}}^2}. \quad (17)$$

Code description: We simulate the GR – Klein-Gordon system using the COSMOS and LEAN-SR codes. Both codes have been designed to solve Einstein’s equations as an initial value problem. Computationally this

results in solving (i) a set of coupled elliptic partial differential equations (PDEs) to provide initial data for BH spacetimes and (ii) a set of coupled hyperbolic-type PDEs for the time evolution. The evolution PDEs are solved using the method of lines employing a 4th order Runge-Kutta time integrator. Spatial components are computed on 3-dimensional, nested Cartesian meshes and (spatial) derivatives are realized by centered or lop-sided finite difference (FD) stencils. While the codes provide FD stencils up to sixth order, in practice we employ centered fourth order FD stencils for regular derivatives (in the interior of the numerical domain) and fourth order lop-sided FD stencils to realize advection derivatives.

The LEAN-SR code is based on the CACTUS computational toolkit [107, 108], part of the EINSTEIN TOOLKIT [109, 110], and Sperhake’s LEAN code [111]. Initial configurations are set up either by using analytic data or by solving the constraints using the spectral TWO PUNCTURES solver [112]. In order to compute the AH we employ the AHFINDERDIRECT [104, 105]. The code furthermore incorporates adaptive mesh refinement (AMR) provided by the CARPET package [113, 114] and uses boxes moving across the numerical domain tracking the motion of the BHs. Parallelization is implemented with MPI.

The algorithm of the COSMOS code is based on the SACRA code written by T. Yamamoto *et al.* [115] and developed to solve binary problems. Initial data is given either analytically or constructed by solving the constraints numerically using the Multi-Grid solver [116]. In order to compute the AH we implement the AH finder based on Refs. [117, 118]. The code employs fixed mesh refinement (FMR) and the BH is located at the center of the computational domain. Parallelization is implemented with OpenMP.

We set up our numerical domain using (fixed or adaptive) mesh refinement. Then, the numerical grid contains N_{RL} refinement levels centered around the BH. We denote the egde length of the $n - th$ refinement level as $2x_n$. Its resolution is given by $h_n = 2^{n-1}h_1$, where h_1 is the resolution of the innermost refinement level. During the presentation of the results we adopt the notation of Sec. II E in Ref. [111] and we summarize the grid setup as

$$\{(x_{N_{RL}}, x_{N_{RL}-1}, \dots, x_1), h = h_1\}. \quad (18)$$

In all tables summarizing the numerical setup we use units in which the BH bare mass $M = 1$ (see Section III, in particular Eqs. (21) and (45)).

III. INITIAL DATA CONSTRUCTION FOR BLACK HOLES IMMERSED IN SCALAR FIELDS

The approach to the time evolution problem outlined in the previous section has to be completed by setting up initial states for the dynamical quantities $(\gamma_{ij}, \Phi_{R,I}, K_{ij}, \Pi_{R,I})$. Any initial data (describing GR

systems) have to be a solution of Einstein’s equations (3) and, therefore, have to satisfy the constraints (8). In general, the construction of these solutions implies solving a set of four coupled, elliptic PDEs which is difficult but nowadays well understood for vacuum spacetimes (see, e.g., Refs. [86, 116, 119] and references therein). However, more brainwork is needed to provide appropriate initial data for the more complicated case that we are interested in and in which BH spacetimes are coupled to scalar fields.

In fact, some, if not all studies dealing with such a system have taken a crude approach and simply superposed a scalar field onto a BH spacetime [120, 121], thus setting up *constraint violating* initial data. However, the consequences of these procedures are not clear and, indeed, might contaminate the entire evolution of a system. Bear in mind, that the constraint violation caused by the presence of the scalar field typically lies outside the BH, i.e., it is not hidden behind a horizon. Furthermore, the employed BSSN evolution scheme does not have any constraint damping mechanism and, thus, their violation will remain present throughout the entire time evolution. The consequences of this argument will be clarified below, when we compare the evolution of constraint-violating and constraint-satisfying initial data, summarized also in Fig. 1.

For this reason it is mandatory to construct appropriate, *constraint satisfying* initial data. We have found novel, generic *analytic* or numerical solutions to this problem which may be very useful to study extensions of GR to include self-interacting fields. Our construction can also prove useful in completely different contexts such as the collapse of self-interacting fundamental fields in scalar-tensor theories or dynamical spacetimes in other modified theories of gravity involving couplings to dilaton or axionic fields. Solving the constraints (a set of four coupled, elliptic PDEs) is in general a demanding task. In order to simplify the problem it is useful to perform a conformal transformation of the ADM variables [119]

$$\gamma_{ij} = \psi^4 \tilde{\gamma}_{ij}, \quad \tilde{\gamma} = \det \tilde{\gamma}_{ij} = 1, \quad (19a)$$

$$K_{ij} = A_{ij} + \frac{1}{3} \gamma_{ij} K, \quad A_{ij} = \psi^{-2} \tilde{A}_{ij}. \quad (19b)$$

Then, the constraints (8) become

$$\mathcal{H} = \tilde{\Delta} \psi - \frac{1}{8} \tilde{R} \psi - \frac{1}{12} K^2 \psi^5 + \frac{1}{8} \tilde{A}^{ij} \tilde{A}_{ij} \psi^{-7} + \pi \psi \left[\tilde{D}^i \Phi^* \tilde{D}_i \Phi + \psi^4 (\Pi^* \Pi + \mu_S^2 \Phi^* \Phi) \right], \quad (20a)$$

$$\mathcal{M}_i = \tilde{D}_j \tilde{A}_i^j - \frac{2}{3} \psi^6 \tilde{D}_i K - 4\pi \psi^6 \left(\Pi^* \tilde{D}_i \Phi + \Pi \tilde{D}_i \Phi^* \right), \quad (20b)$$

in terms of the conformal variables, where $\tilde{\Delta} = \tilde{\gamma}^{ij} \tilde{D}_i \tilde{D}_j$ and \tilde{D} and \tilde{R} denote the conformal covariant derivative and Ricci scalar. Note, that the constraints (20) fix four of the 16 independent variables $(\psi, \tilde{\gamma}_{ij}, \tilde{A}_{ij}, K, \Phi_{R,I}, \Pi_{R,I})$ at $t = 0$. This leaves the freedom to specify the remaining quantities motivated by the physical scenario under consideration and allowing for further simplifications of the PDE problem.

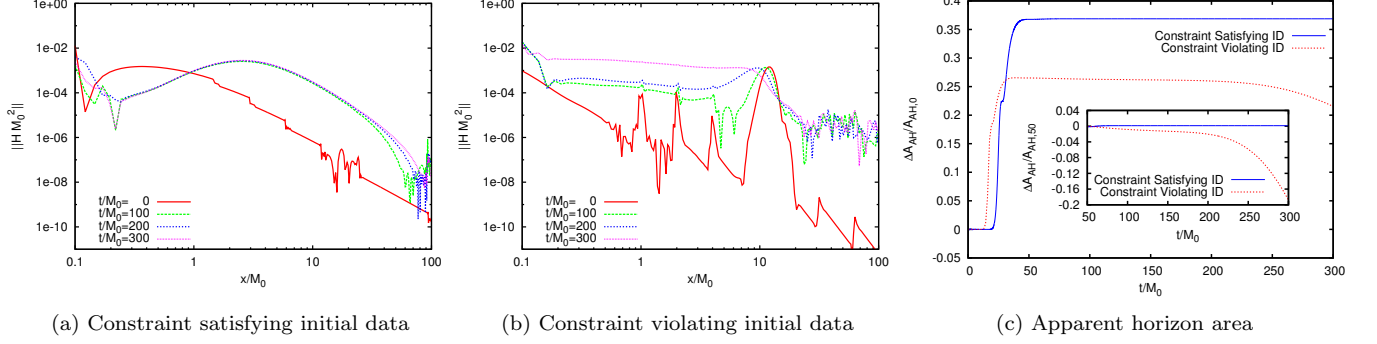


FIG. 1. Evolution of constraint satisfying (left panel, for further details on the construction see Table I and section III A) and constraint violating (mid) initial data, corresponding to run *S00_m0_e* and *S00_CV* in Table I. In both cases the spherically symmetric scalar shells are located at $r_0 = 12M$ with a width of $w = 2M$ and amplitude $MA = 0.075$. Figs. (a) and (b) show the Hamiltonian constraint along the x -axis at different times throughout the evolution. Constraints become violated with larger magnitude at late times for constraint-violating initial data, specially close to the horizon. At late-times this impacts on physical quantities such as the AH area, shown in Fig. (c), where $A_{AH,t}$ denotes the AH area at time t . The violation of the constraints causes the AH area to *decrease* (red dotted line) violating the area theorem while this unphysical feature does not occur with constraint satisfying initial data (blue solid line). The inset normalizes the area variation to zero at $t = 50$, in order to better gauge the changes induced by both types of initial data.

A. Non-rotating black holes: analytic initial data

We start by considering a single, non-rotating BH surrounded by a scalar field. The line element of the Schwarzschild BH in isotropic coordinates is given by

$$ds^2 = - \left(\frac{1 - \frac{M}{2r}}{1 + \frac{M}{2r}} \right)^2 dt^2 + \left(1 + \frac{M}{2r} \right)^4 \eta_{ij} dx^i dx^j \\ = - \alpha^2 dt^2 + \psi_S^4 \eta_{ij} dx^i dx^j, \quad (21)$$

where M is the BH bare mass parameter and r is the isotropic, radial coordinate. We impose conformal flatness, i.e., $\tilde{\gamma}_{ij} = \eta_{ij}$ and set $\tilde{A}_{ij} = 0$, because the BH has neither linear nor angular momentum. Then, the constraints (20) become

$$0 = \Delta_{\text{flat}} \psi - \frac{1}{12} K^2 \psi^5 + \pi \psi \eta^{ij} (\partial_i \Phi_R \partial_j \Phi_R + \partial_i \Phi_I \partial_j \Phi_I) \\ + \pi \psi^5 [(\Pi_R^2 + \Pi_I^2) + \mu_S^2 (\Phi_R^2 + \Phi_I^2)], \quad (22a)$$

$$0 = \partial_i K + 6\pi (\Pi_R \partial_i \Phi_R + \Pi_I \partial_i \Phi_I), \quad (22b)$$

where Δ_{flat} is the flat space Laplacian. Note, that we cannot specify $K = 0$ and $\psi = \psi_S$ simultaneously because then the Hamiltonian constraint (8a) would not be satisfied for an arbitrary non-zero scalar field surrounding a Schwarzschild BH. Here, we adopt the maximal slicing condition $K = 0$ and solve for deformations of the conformal factor from the Schwarzschild case. With these specifications the momentum constraint (22b) implies that at $t = 0$ either Π should vanish or Φ should be a constant. We consider the latter case and, specifically, choose $\Phi = 0$. Then, the momentum constraint (22b) is satisfied trivially and the Hamiltonian constraint (22a)

in spherical coordinates becomes

$$\Delta_{\text{flat}} \psi = \left[\frac{1}{r^2} \frac{\partial}{\partial r} r^2 \frac{\partial}{\partial r} + \frac{1}{r^2 \sin \theta} \frac{\partial}{\partial \theta} \sin \theta \frac{\partial}{\partial \theta} + \frac{1}{r^2 \sin^2 \theta} \frac{\partial^2}{\partial \phi^2} \right] \psi \\ = - \pi \psi^5 (\Pi_R^2 + \Pi_I^2). \quad (23)$$

The ansatz

$$\Pi = \frac{\psi^{-5/2}}{\sqrt{r\pi}} F(r) Z(\theta, \phi), \quad (24a)$$

$$\psi = \psi_S + \sum_{lm} \frac{u_{lm}(r)}{r} Y_{lm}(\theta, \phi) \\ = 1 + \frac{M}{2r} + \sum_{lm} \frac{u_{lm}(r)}{r} Y_{lm}(\theta, \phi), \quad (24b)$$

reduces the Hamiltonian constraint to

$$\sum_{lm} \left(u_{lm}'' - \frac{l(l+1)}{r^2} u_{lm} \right) Y_{lm} = - F(r)^2 Z(\theta, \phi)^2, \quad (25)$$

where we (furthermore) impose that $Z(\theta, \phi)$ and ψ are real functions. Thus, we have been able to reduce a complex problem to finding the solution of an inhomogenous second order ordinary differential equation (ODE). This equation has a number of interesting analytic solutions. Here, we focus on two different classes of Gaussian-type initial conditions, one of which is spherically symmetric, while the second class contains a dipole configuration:

Initial data I: Let us start with Gaussian-type, spherically symmetric initial data,

$$Z(\theta, \phi) = \frac{1}{\sqrt{4\pi}}, \quad F(r) = A_{00} \times \sqrt{r} e^{-\frac{(r-r_0)^2}{w^2}}, \quad (26)$$

where A_{00} is the scalar field amplitude and r_0 and w are the location of the centre of the Gaussian and its width.

By solving Eq. (25), we obtain the only non-vanishing component of $u_{lm}(r)$

$$u_{00} = A_{00}^2 \frac{w(w^2 - 4r_0(r - r_0))}{16\sqrt{2}} \left(\operatorname{erf} \left(\frac{\sqrt{2}(r - r_0)}{w} \right) - 1 \right) - A_{00}^2 \frac{r_0 w^2}{8\sqrt{\pi}} e^{-2(r-r_0)^2/w^2}, \quad (27)$$

where we have imposed that $u_{lm} \rightarrow 0$ at infinity. Other solutions can be obtained by adding a constant to (27).

Initial data II: The second case of interest concerns initial data for a dipole scalar field². Specifically, we consider a superposition of $l = 1, m = \pm 1$ spherical harmonics for its angular dependency, such that $Z(\theta, \phi) \in \mathbb{R}$

and set

$$Z(\theta, \phi) = Y_{1-1} - Y_{11} = \sqrt{\frac{3}{2\pi}} \sin \theta \cos \phi, \quad (28a)$$

$$F(r) = A_{11} \times r e^{-\frac{(r-r_0)^2}{w^2}}. \quad (28b)$$

As before r_0 and w are the parameters of the Gaussian, whereas A_{11} denotes the amplitude of the dipole scalar field. The only non-vanishing Clebsch-Gordon coefficients $C_Y^{lm} \equiv \int d\Omega Z(\theta, \phi)^2 Y_{lm}(\theta, \phi)$ are

$$C_Y^{00} = \frac{1}{\sqrt{\pi}}, \quad C_Y^{20} = -\frac{1}{\sqrt{5\pi}}, \quad C_Y^{22} = C_Y^{2-2} = \sqrt{\frac{3}{10\pi}}. \quad (29)$$

We thus find the following ODE for u_{lm}

$$u_{lm}'' - \frac{l(l+1)}{r^2} u_{lm} = -C_Y^{lm} F(r)^2, \quad (30)$$

with non-vanishing contributions

$$u_{22} = u_{2-2} = -\frac{A_{11}^2 w^2}{80r^2} \sqrt{\frac{3}{10\pi}} e^{-2\frac{(r-r_0)^2}{w^2}} (4(r^4 + r^3 r_0 + r^2 r_0^2 + r r_0^3 + r_0^4) + w^2(4r^2 + 7r r_0 + 9r_0^2) + 2w^4) + A_{11}^2 \sqrt{\frac{3}{5}} \frac{w(-16r^5 + 16r_0^5 + 40r_0^3 w^2 + 15r_0 w^4)}{320r^2} \left(\operatorname{erf} \left(\frac{\sqrt{2}(r-r_0)}{w} \right) - 1 \right) + A_{11}^2 \sqrt{\frac{3}{5}} \frac{w r_0 (16r_0^4 + 40r_0^2 w^2 + 15w^4)}{320r^2} \left(\operatorname{erf} \left(\frac{\sqrt{2}r_0}{w} \right) + 1 \right) + A_{11}^2 \sqrt{\frac{6}{5\pi}} e^{-2r_0^2/w^2} \frac{2w^2(4r_0^4 + 9r_0^2 w^2 + 2w^4)}{320r^2}, \quad (31a)$$

$$u_{00} = \frac{A_{11}^2 w}{16} \left(-\frac{2w(2r_0^2 + w^2)e^{-2(r-r_0)^2/w^2}}{\sqrt{\pi}} - \sqrt{2} (4(r - r_0)r_0^2 + (r - 3r_0)w^2) \left(\operatorname{erf} \left(\frac{\sqrt{2}(r-r_0)}{w} \right) - 1 \right) \right), \quad (31b)$$

$$u_{20} = -\sqrt{\frac{2}{3}} u_{22}. \quad (31c)$$

Comparison of constraint-satisfying and constraint-violating initial data: To gauge the usefulness of this initial data, we have compared the evolution of both constraint violating and constraint satisfying setups, runs *S00_CV* and *S00_m0_e* in Table I, respectively. In both cases we considered a spherically symmetric scalar field surrounding an initially non-rotating BH. The massless scalar shell is localized around $r_0 = 12M$ with a width of $w = 2.0M$ and amplitude $MA = 0.075$. This constraint-violating initial data closely resembles the setup used in Refs. [120, 121].

² Note, that the scalar field momentum Π is *never* a pure dipole, because the term in Eq. (24a) that is proportional to the conformal factor ψ mixes multipoles. For all practical purposes, we will refer to this configuration as “dipole” bearing in mind this caveat.

Figs. 1a and 1b show snapshots of the Hamiltonian constraint along the x-axis. We find that constraint violating initial data evolves to solutions which violate the constraints even more severely with time. This is particularly relevant close to the horizon, and it leads to unphysical properties, such as a strong *decrease* in the AH area as illustrated in Fig. 1c. We note that this violates the first law of BH thermodynamics, which states that the area of the (event) horizon should always increase. On the other hand, the analytic, constraint-satisfying initial data yields much better constraint-preserving evolutions, leading to physically sensible results, as is apparent in Fig. 1c.

Validation of constraint satisfying initial data: Additionally, we have performed a series of simulations constructing both type-I and type-II initial data for different sets (r_0, w) of scalar field parameters and a wide range of amplitudes. In Fig. 2 we show the relation between the

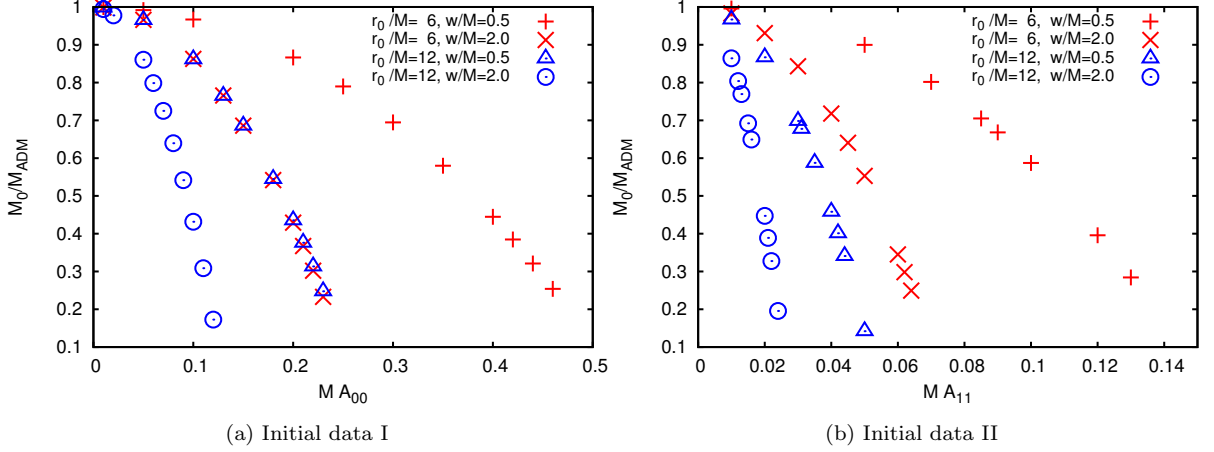


FIG. 2. We present the relation between the initial BH mass $M_0 = M_{\text{BH}}(0)$ normalized by the ADM mass, and the scalar field amplitude A_{lm} for initial data I (left) and II (right) for various sets of parameters. Specifically, the Gaussian scalar shells with widths $w = 0.5M$ or $w = 2.0M$ are centered around $r_0 = 6M$ or $r_0 = 12M$. The BH mass decreases as the amplitude increases because we have fixed the ADM mass.

scalar field amplitude and the BH mass at $t = 0$. The total (ADM) mass M_{ADM} is fixed in these constructions because the term $\sum_{lm} \frac{u_{lm}}{r} Y_{lm}$ in the conformal factor (24b) falls off sharply at infinity and we have required $u_{lm} \rightarrow 0$ asymptotically. Therefore, the correction to the conformal factor, Eq. (24b), does not contribute to the mass of the system. Both initial data sets have similar qualitative features, and specifically the BH Christodoulou mass decreases as the amplitude of the scalar field increases.

B. Extensions to generic conformally flat spacetimes and other scalar field profile

We note, that in the previous construction we considered scalar clouds around a spherically symmetric spacetime with fixed ADM mass M_{ADM} by requiring that u_{lm} vanishes asymptotically. However, this is only one possible choice. In particular, the framework is valid as long as we assume a conformally flat metric and can, therefore, easily be extended to more general cases.

The simplest example is the Minkowski spacetime with line element

$$ds^2 = -dt^2 + \eta_{ij} dx^i dx^j, \quad (32)$$

for which $\tilde{\gamma}_{ij} = \eta_{ij}$ and $K = 0$ by construction. Again, we choose $\Phi = 0$ and adopt Eq. (24a) for the scalar field momentum. Because initially there is no BH present in this spacetime we take the ansatz

$$\psi = 1 + \sum_{lm} \frac{u_{lm}}{r} Y_{lm}(\theta, \phi), \quad (33)$$

for the conformal factor, which follows directly from Eq. (24b) in the limit $M \rightarrow 0$. Then, the Hamiltonian constraint results in the ODE given in Eq. (25). This

implies that the solutions u_{lm} of the initial data I and II are also the analytic solutions for the Minkowski “background” spacetimes with the ansatz (26) and (28). We note that, in particular, the solution with the ansatz (26) is spherically symmetric and the dynamical problem can be reduced to a 1 + 1 problem [122]. In this case, the solution is written with u_{00} given in Eq. (27) by

$$\psi = 1 + \frac{u_{00}(r) - u_{00}(0)}{2r\sqrt{\pi}}, \quad (34a)$$

$$\Pi = \frac{A_{00}}{2\pi} e^{-\frac{(r-r_0)^2}{w^2}} \psi^{-\frac{5}{2}}, \quad (34b)$$

where we subtracted $u_{00}(0)$ in order to regularize the conformal factor at the origin (because $u_{00}(0)$ is a nonzero constant, making the term $u_{00}(r)/r$ singular at the origin). The system has ADM energy $M_{\text{ADM}} = -u_{00}(0)/\sqrt{\pi}$ due to the scalar field.

C. Superposition of scalar field profiles and multiple black holes

Another interesting setup would be the superposition of various scalar fields motivated by the possible presence of more than one fundamental, ultralight scalar field or by the prospect of coupling fundamental fields to spacetimes in modified gravity, such as scalar–tensor theories. Here, we will focus on scalar clouds in Minkowski or around Schwarzschild BHs which allows us to provide analytic solutions describing this setup. In particular, we can keep the assumptions that we made in the last section, namely

$$\tilde{\gamma}_{ij} = \eta_{ij}, \quad K = 0, \quad \Phi = 0. \quad (35)$$

Instead, we consider non-trivial profiles of the scalar field momenta and will solve the Hamiltonian constraint for

the deformation of the conformal factor from its value ψ_{CF} in the absence of any additional field. In particular, for Minkowski we have $\psi_{\text{CF}} = 1$. In a spacetime containing N_{BH} non-rotating BHs without any momenta the solution is given by Brill-Lindquist initial data [123, 124]

$$\psi_{\text{CF}} = 1 + \sum_{(a)=1}^{N_{\text{BH}}} \frac{M_{(a)}}{2r_{(a)}}, \quad (36)$$

where $M_{(a)}$ and $r_{(a)}$ are the bare mass parameter and position of the (a) -th BH. For example, the calculation of the previous section can be generalized to two spherically symmetric profiles (with equal amplitude),

$$\Pi = \Pi_1 + \Pi_2, \quad \Pi_i = \frac{A_{00}}{2\pi} e^{-\frac{(r-r_i)^2}{w^2}} \psi^{-\frac{5}{2}}, \quad (37)$$

where r_i denotes the distance of the peak of the i -th spherical shell from the origin. We take the ansatz for the conformal factor

$$\psi = \psi_{\text{CF}} + \left[u_{00,1} + u_{00,2} + u_{00,\text{CF}} \right] \frac{Y_{00}(\theta, \phi)}{r}. \quad (38)$$

Although the Hamiltonian constraint becomes more complicated with this ansatz we already know the solution of the following equations by choosing appropriate parameters in Eq. (27),

$$\Delta_{\text{flat}} \frac{u_{00,i}(r; A_{00}, r_i)}{r} Y_{00} = -\pi \psi^5 \Pi_i^2. \quad (39)$$

The solution of the remaining equation can be described by the parameters \bar{A}_{00} and \bar{r}_{12} ,

$$\begin{aligned} \Delta_{\text{flat}} \frac{u_{00,\text{CF}}(r; \bar{A}_{00}, \bar{r}_{12})}{r} Y_{00} &= -2\pi \psi^5 \Pi_1 \Pi_2 \\ &= -\frac{\bar{A}_{00}^2}{4\pi} e^{-\frac{2(r-\bar{r}_{12})^2}{w^2}}, \end{aligned} \quad (40)$$

where

$$\bar{A}_{00}^2 = 2A_{00}^2 e^{-\frac{(r_1-r_2)^2}{2w^2}}, \quad \bar{r}_{12} = \frac{r_1 + r_2}{2}. \quad (41)$$

Thus, the initial data describing the superposition of two scalar fields is given by

$$\begin{aligned} \psi &= \psi_{\text{CF}} + \frac{1}{2r\sqrt{\pi}} \left[u_{00,1}(r; A_{00}, r_1) - u_{00,1}(0; A_{00}, r_1) \right. \\ &\quad + u_{00,2}(r; A_{00}, r_2) - u_{00,2}(0; A_{00}, r_2) \\ &\quad \left. + u_{00,\text{CF}}(r; \bar{A}_{00}, \bar{r}_{12}) \right], \end{aligned} \quad (42a)$$

$$\Pi = \frac{A_{00}}{2\pi} \psi^{-\frac{5}{2}} \left[e^{-\frac{(r-r_1)^2}{w^2}} + e^{-\frac{(r-r_2)^2}{w^2}} \right]. \quad (42b)$$

In addition, one can extend this construction to N_{SF} scalar field profiles in a straight-forward calculation

$$\begin{aligned} \psi &= \psi_{\text{CF}} + \frac{1}{2r\sqrt{\pi}} \left[\sum_{i=1}^{N_{\text{SF}}} \{ u_{00,i}(r; A_{00}, r_i) - u_{00,i}(0; A_{00}, r_i) \} \right. \\ &\quad \left. + \sum_{i < j} u_{00,ij}(r; \bar{A}_{00,ij}, \bar{r}_{ij}) \right], \end{aligned} \quad (43a)$$

$$\Pi = \frac{A_{00}}{2\pi} \psi^{-\frac{5}{2}} \sum_{i=1}^{N_{\text{SF}}} e^{-\frac{(r-r_i)^2}{w^2}}, \quad (43b)$$

with

$$\bar{A}_{00,ij}^2 = 2A_{00}^2 e^{-\frac{(r_i-r_j)^2}{2w^2}}, \quad \bar{r}_{ij} = \frac{r_i + r_j}{2}, \quad (44)$$

where the constant $u_{00,i}(r=0)$ was added to $u_{00,i}(r)$ in order to have a positive ADM mass. In principle, it is possible to generalize the construction outlined in this section to include type II initial data, modeling the superposition of N_{SF} dipole scalar fields, or to allow for arbitrary amplitude $A_{i,00} \neq A_{j,00}$.

D. A rotating black hole surrounded by a scalar field

A particularly interesting scenario that we have not yet captured with our analytic initial data construction are scalar fields surrounding rotating BHs. This is an especially attractive setup, because it opens up the possibility to explore superradiant effects and the BH bomb mechanism *non-linearly*. For this purpose we consider the Kerr solution as underlying BH spacetime. The line element of the Kerr BH in Boyer-Lindquist (BL) coordinates is given by

$$\begin{aligned} ds^2 &= - \left(1 - \frac{2Mr_{\text{BL}}}{\Sigma} \right) dt^2 - \frac{4aMr_{\text{BL}} \sin^2 \theta}{\Sigma} dt d\phi \\ &\quad + \frac{\Sigma}{\Delta} dr_{\text{BL}}^2 + \Sigma d\theta^2 + \frac{\mathcal{A}}{\Sigma} \sin^2 \theta d\phi^2, \end{aligned} \quad (45a)$$

$$\mathcal{A} = (r_{\text{BL}}^2 + a^2)^2 - \Delta a^2 \sin^2 \theta, \quad (45b)$$

$$\Sigma = r_{\text{BL}}^2 + a^2 \cos^2 \theta, \quad (45c)$$

$$\Delta = r_{\text{BL}}^2 - 2Mr_{\text{BL}} + a^2, \quad (45d)$$

where M is again the BH bare mass parameter and a/M is the dimensionless spin parameter. However, BL coordinates are not favourable from a numerical viewpoint, because there are coordinate singularities at the location of horizon $r_{\pm} = M \pm \sqrt{M^2 - a^2}$. Brandt & Seidel [125, 126] and Liu et al [83] proposed to employ quasi-isotropic coordinates in which the spatial metric components remain regular. Following Liu et al [83], we introduce the quasi-isotropic radial coordinate R which is related to the BL radial coordinate r_{BL} via

$$r_{\text{BL}} = R \left(1 + \frac{r_{\pm}}{4R} \right)^2. \quad (46)$$

In this coordinate the outer horizon is located at $R = \frac{r_+}{4}$ which results in a *finite* value $\lim_{a/M \rightarrow 1} R = \frac{M}{4}$ in the extremal limit. Thus, we are able to stably evolve highly spinning BHs – with initial spin up to $a_0/M \sim 0.95$ – represented by punctures with high accuracy. To be precise, the deviation from the expected spin parameter (in the pure Kerr case) is less than 1% even for the highest spinning case, as we will discuss in Appendix B (see also Ref. [83]). In these quasi-isotropic coordinates (R, θ, ϕ) the spatial part of the Kerr solution (45) writes

$$\begin{aligned} dl^2 &= \gamma_{ij}^{\text{BG}} dx^i dx^j \\ &= \psi_0^4 \left[\frac{(R + \frac{r_+}{4})^2}{R(r_{\text{BL}} - r_-)} dR^2 + R^2 d\theta^2 + \frac{\mathcal{A}}{\Sigma^2} R^2 \sin^2 \theta d\phi^2 \right], \\ \tilde{\gamma}_{ij}^{\text{BG}} &= \psi_0^{-4} \gamma_{ij}^{\text{BG}}, \quad \psi_0^4 = \frac{\Sigma}{R^2}, \\ \alpha &= \sqrt{\frac{\Delta \Sigma}{\mathcal{A}}}, \quad \beta^\phi = -2aM \frac{r_{\text{BL}}}{\mathcal{A}} \end{aligned} \quad (47)$$

where \mathcal{A} , Σ and Δ are given by Eqs. (45). The extrinsic curvature becomes

$$\begin{aligned} K_{R\phi}^{\text{BG}} &= \frac{aM \sin^2 \theta}{\Sigma \sqrt{\mathcal{A} \Sigma}} (2r_{\text{BL}}^2 [r_{\text{BL}}^2 + a^2] + \Sigma [r_{\text{BL}}^2 - a^2]) \\ &\quad \times \left(1 + \frac{r_+}{4R} \right) \frac{1}{\sqrt{R} \sqrt{r_{\text{BL}} - r_-}}, \end{aligned} \quad (48a)$$

$$\begin{aligned} K_{\theta\phi}^{\text{BG}} &= -2a^3 M \frac{r_{\text{BL}} \cos \theta \sin^3 \theta}{\Sigma \sqrt{\mathcal{A} \Sigma}} \\ &\quad \times \left(1 - \frac{r_+}{4R} \right) \sqrt{R} \sqrt{r_{\text{BL}} - r_-}. \end{aligned} \quad (48b)$$

Let us now consider the presence of a scalar field around a Kerr BH. In order to prepare this type of configuration properly we need to solve the constraint Eqs. (20). Specifically, we adopt the Kerr metric in quasi-isotropic coordinates, Eq. (47), as conformal metric with the curvature given in Eq. (48). We still have the freedom to impose the maximal slicing condition and, furthermore, choose a vanishing scalar field initially, yielding the ansatz

$$K = 0, \quad \Phi = 0, \quad \Pi = \frac{A_G}{\sqrt{\pi}} \psi^{-\frac{5}{2}} Z(\theta, \phi) e^{-\frac{(r-r_0)^2}{w^2}} \quad (49)$$

where the different angular profiles $Z(\theta, \phi)$ are given in Eqs. (26) or (28). The constraint Eqs. (20) become

$$\mathcal{H} = \tilde{\Delta} \psi - \frac{1}{8} \tilde{R}^{\text{BG}} \psi + \frac{1}{8} \tilde{A}_{\text{BG}}^{ij} \tilde{A}_{ij}^{\text{BG}} \psi^{-7} + \pi \Pi^2 \psi^5 = 0, \quad (50a)$$

$$\mathcal{M}_i = \tilde{D}_j \tilde{A}^{\text{BG}j}_i = 0, \quad (50b)$$

where \tilde{R}^{BG} corresponds to $\tilde{\gamma}_{ij}^{\text{BG}}$ in Eq. (47) and the traceless extrinsic curvature of the Kerr BH is defined by using background quantities as $\tilde{A}_{ij}^{\text{BG}} = \psi_0^2 K_{ij}^{\text{BG}}$. As long as we use the background conformal metric and the traceless component of the background extrinsic curvature, the momentum constraints (20b) are trivially satisfied

by the maximal slicing condition. Furthermore, we take the ansatz for the conformal factor

$$\psi \equiv \psi_0 (1 + u(r, \theta, \phi)), \quad (51)$$

where ψ_0 is given in Eq. (47). Then, Eq. (50a) becomes

$$\begin{aligned} \Delta_{\text{flat}} u &= \left[\eta^{ij} - \tilde{\gamma}_{\text{BG}}^{ij} \right] \partial_i \partial_j u - \tilde{\gamma}_{\text{BG},i}^{ij} \partial_j u \\ &\quad - 2 \tilde{\gamma}_{\text{BG}}^{ij} \psi_0^{-1} \partial_i u \partial_j \psi_0 - A_G^2 \psi_0^{-1} Z^2(\theta, \phi) e^{-\frac{2(r-r_0)^2}{w^2}} \\ &\quad + \frac{1}{8} \tilde{A}_{\text{BG}}^{ij} \tilde{A}_{ij}^{\text{BG}} \psi_0^{-8} u(2+u)(2+2u+u^2) \\ &\quad \times (2+4u+6u^2+4u^3+u^4)(1+u)^{-7}, \end{aligned} \quad (52)$$

where we have used the vacuum Hamiltonian constraint to eliminate the Ricci scalar \tilde{R}^{BG} . As we have shown, this procedure yields a single elliptic PDE for the regular function u which we will solve numerically using standard numerical methods under the outer boundary condition $u \rightarrow r^{-1}$.

E. A black hole and a pseudo-bound state of a scalar field

We have just explored different ways of providing initial data either in closed analytic form or requiring numerical integrations assuming Gaussian scalar field profiles. However elegant and appealing, these constructions still describe very contrived physical situations. Accordingly, the time evolution of these initial conditions might lead to arbitrary, potentially large absorption and scattering of radiation to infinity.

However, linearized perturbations of massive scalar fields around Kerr BHs have revealed the existence of long-lived modes, or quasi-bound states, which have been investigated in the frequency domain in the past [50–52, 127]. The quasi-bound states are useful because they prescribe a clean state and, in fact, numerical simulations in the time domain have uncovered interesting phenomena [38, 57, 58].

We now turn to the question of constructing initial data that corresponds roughly to the scenario under consideration, i.e., describing long-lived quasi-stationary states around BHs, for which the scalar field is almost monochromatic and in a very specific angular momentum state. We will call this initial data *pseudo-bound states*, as they will solve the full non-linear problem but only mimic the *quasi-bound states* seen in linearized studies [34, 37, 38]. The evolution of this data will lead to very small initial accretion or loss to infinity.

Initial data describing pseudo-bound states requires both a non-vanishing scalar field Φ and conjugated momentum Π . In this case the momentum constraints (20b) become (in principle) non-trivial and are difficult to solve even numerically. We show how to lighten this burden

by taking the ansatz for Φ ³

$$\Phi(t, r, \theta, \phi) = \frac{A_P}{\sqrt{\pi}} \exp \left[i(\omega t + m\phi) - \frac{(r-r_0)^2}{w^2} \right] Z(\theta), \quad (53)$$

where r_0 and w are the location and width of the Gaussian and A_P is the scalar field amplitude. We get, by definition, the relation,

$$\Pi(t, r, \theta, \phi) = \frac{1}{\alpha} [\beta \partial_\phi \Phi - \partial_t \Phi] = \frac{i}{\alpha} (m\beta - \omega) \Phi, \quad (54)$$

where we defined $\beta = \beta^\phi$. We now insert Eq. (54) into the momentum constraints (20b) and recall that $\tilde{A}^{\text{BG}j}_i$ solves the vacuum momentum constraints. Then, Eq. (20b) yields the relation

$$\begin{aligned} \partial_i K &= -6\pi [\Pi \partial_i \Phi^* + \Pi^* \partial_i \Phi] \\ &= -i \frac{6\pi(m\beta - \omega)}{\alpha} [\Phi \partial_i \Phi^* - \Phi^* \partial_i \Phi] \\ &= -\frac{12\pi A_P^2}{\alpha} (m\beta - \omega) e^{-\frac{(r-r_0)^2}{w^2}} Z(\theta)^2 \delta_i^\phi. \end{aligned} \quad (55)$$

Here, we solve the (momentum) constraints (20b) by imposing the minimal slicing condition, i.e., $\partial_i K = 0$. Then, the relation (55) implies that $m\beta = \omega$ must hold. Naively, one could fix the frequency $\omega = \omega_B = \text{const}$ to be the characteristic frequency of a quasi-bound state. However, $\beta = \text{const}$ would not be consistent with demanding asymptotic flatness as well as the requirement that the shift vector decreases sufficiently fast at large distances. Therefore, it is convenient to consider a position dependent shift and, consequently, a position dependent frequency $\omega/m = \beta$, such that Eq. (55) remains satisfied. Guided by perturbative studies we relate the space-dependent frequency ω to the characteristic frequency ω_B of quasi-bound states (which is always of the order of the mass of the field), and specifically we set

$$\begin{aligned} \beta(r, \theta, \phi) \Big|_{t=0} &= \frac{\omega(r, \theta, \phi)}{m} \\ &= \frac{\omega_B}{m} \sqrt{\frac{3}{2\pi}} \exp \left[-\frac{(r-r_0)^2}{w^2} \right] \sin \theta \cos \phi. \end{aligned} \quad (56)$$

We now substitute the metric (47) and the extrinsic curvature (48) in the Hamiltonian constraint (20a), and obtain

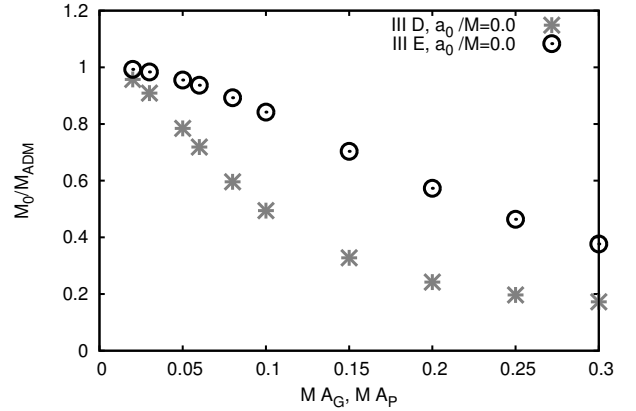
$$\begin{aligned} \mathcal{H} &= \tilde{\Delta} \psi - \frac{1}{8} \tilde{R}^{\text{BG}} \psi + \frac{1}{8} \tilde{A}^{\text{BG}ij}_{\text{BG}} \tilde{A}^{\text{BG}}_{ij} \psi^{-7} \\ &\quad + \pi \psi \tilde{\gamma}^{\text{BG}ij}_{\text{BG}} \tilde{D}_i \Phi \tilde{D}_j \Phi^* + \pi \mu_S^2 \psi^5 \Phi \Phi^* = 0. \end{aligned} \quad (57)$$

Note, that now the initial data depends on the mass parameter μ_S . In addition, we split the conformal factor according to Eq. (51) and eliminate the Ricci scalar term using the vacuum Hamiltonian. Under these conditions

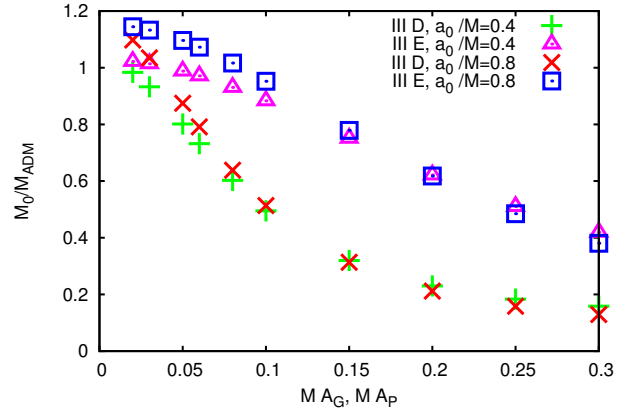
we end up with a single elliptic PDE for the regular function u

$$\begin{aligned} \Delta_{\text{flat}} u &= \left[\eta^{ij} - \tilde{\gamma}^{\text{BG}ij}_{\text{BG}} \right] \partial_i \partial_j u - \tilde{\gamma}^{\text{BG}ij}_{\text{BG},i} \partial_j u - 2\tilde{\gamma}^{\text{BG}ij}_{\text{BG}} \psi_0^{-1} \partial_i u \partial_j \psi_0 \\ &\quad + \frac{1}{8} \tilde{A}^{\text{BG}ij}_{\text{BG}} \tilde{A}^{\text{BG}}_{ij} \psi_0^{-8} u(2+u)(2+2u+u^2) \\ &\quad \times (2+4u+6u^2+4u^3+u^4)(1+u)^{-7} \\ &\quad - \pi(1+u) \tilde{\gamma}^{\text{BG}ij}_{\text{BG}} (\Phi^R_{,i} \Phi^R_{,j} + \Phi^I_{,i} \Phi^I_{,j}) \\ &\quad - \pi \mu_S^2 \psi_0^4 (1+u)^5 (\Phi^R \Phi^R + \Phi^I \Phi^I). \end{aligned} \quad (58)$$

We can now solve the PDE (58) for u by employing standard numerical methods such as a multigrid or spectral solver.



(a) Non-rotating BH Initial Data



(b) Rotating BH Initial Data

FIG. 3. The relation between the amplitude of a scalar field and the initial BH mass for a non-rotating (top) and rotating BH (bottom). The BH mass (in units of the ADM mass) decreases as the scalar field amplitude increases. Fig. (a) and Fig. (b) show a dipole Gaussian or pseudo-bound state scalar field coupled to a non-rotating BH and a rotating BH with $a_0/M = 0.4$ and 0.8 . The Gaussian scalar wave packet is localized at $r_0 = 12M$ and has width $w = 2M$.

We have checked our initial data implementation by constructing Gaussian or pseudo-bound state scalar clouds using the formalism presented in Sec. III D and III E. In particular we have computed the initial

³ for convenience we use the opposite sign in the time dependence as compared to standard conventions [52].

states of scalar shells with width $w = 2M$ and localized at $r_0 = 12M$ for both non-rotating and rotating BH spacetimes. We present the relation between the BH mass and the amplitude of the scalar cloud in Fig. 3 for various values of the BH spin. The present construction always yields a BH solution for any scalar field amplitude.

IV. RESULTS I – SCALAR CLOUDS AROUND NON-ROTATING BLACK HOLES

This section is devoted to the analysis of scalar clouds interacting with an initially non-rotating BH. We note that even though superradiance is absent in this case, long-lived modes of massive fields still exist, thus involving a potentially rich phenomenology.

The numerical error is estimated to be at most 6% for the scalar and gravitational waveforms at late times while the BH mass, area and spin have at most a $(0.19, 8.5 \cdot 10^{-3}, 0.16)\%$ error. A discussion of the error and convergence analysis is done in Appendix A.

A. Massless scalars around non-rotating black holes

We start by investigating massless scalars coupled to a Schwarzschild BH. Therefore, we set up initial data describing a spherically symmetric or dipole scalar field provided, respectively, by *Initial data I* and *Initial data II* in Sec. III A, Eqs. (27) and (31). We have performed a series of simulations with varying location r_0/M , width w/M and amplitude MA of the Gaussian wave packet, where A refers to the amplitude A_{00} or A_{11} for type I or II initial data in Sec. III A. The specific type and set of parameters of the initial scalar, the mass $M_0 = M_{\text{BH}}(0)$ of the initial BH as well as the grid setup of our numerical domain are summarized in Table I.

We have evolved these configurations in time, following the infall of the scalar shell into the non-rotating BH and their interaction and monitoring the BH's response. Our simulations allow us to explore effects of backreaction onto the spacetime, one effect of which is BH mass increase via scalar field accretion. Depending on the initial energy content of the scalar field we find that the BH mass increases by up to 21% (for our setups) as is illustrated in the top panel of Fig. 4a.

Accretion is generically accompanied by BH ringdown – both in the scalar and the GW channel – which we find is in good agreement with linearized BH perturbation calculations [52]. For spherically symmetric profiles there is no gravitational signal due to the symmetry and the scalar waveform exhibits a short quasi-normal ringdown followed by a power-law fall-off t^{-p} with $p = 3.2$ which is in good agreement with linearized calculations of the power-law tail [128–130]. Instead, the response to the dipole scalar field consists of scalar as well as gravitational quasi-normal ringdown as is shown in Fig. 4b

where we present the respective dominant multipoles Φ_{11} and $\Psi_{4,22}$. As illustrated in Fig. 4a even this apparently simple configuration exposes new features of the BH response: the BH is distorted by the infalling scalar wave and experiences a small spin-up especially from the dipole scalar as can be seen in the bottom panel of Fig. 4a. The excited BH rings down, shedding off most of the angular momentum and settles down to a Kerr BH with a small spin and larger final mass.

B. Massive scalars around non-rotating black holes

We next focus on the time evolution of massive scalar fields around non-rotating BHs. Although this system is not subject to superradiant amplification, it does give rise to long-lived scalar clouds, as illustrated in an animation available at [131] and Fig. 14 in Appendix C, which continuously feed the BH and trigger long-lived GW emission. Thus, even this simple configuration allows for interesting new phenomenology concerning smoking gun effects for “gravitational atoms.” We take as initial data the construction outlined in Sec. III A, Eqs. (27) and (31). Table II summarizes the initial parameters. Throughout this section, we will mainly present results obtained for the scalar field with the largest energy content resulting in a mass coupling $M_0\mu_S = 0.29$.

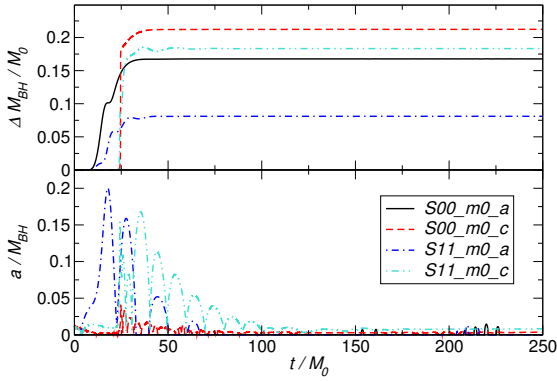
The BH response to a spherically symmetric configuration is summarized in Fig. 5a. A fraction of the field is accreted by the BH, leading to an increase in BH mass of 24%. The infalling scalar excites monopole BH ringdown, shown in Fig. 5b. The short quasinormal ringdown of the $l = m = 0$ mode is succeeded by a late-time power law tail of the form $t^{-p} \sin(\omega t)$ with $p = 0.83$ as illustrated by the red dashed line in Fig. 5b. This numerical value is in excellent agreement with predictions of $p = \frac{5}{6}$ from the linearized analysis of massive scalar fields in BH spacetimes [58, 132–135]. It is remarkable, and to the best of our knowledge the first time, that this late-time massive tail is recovered with such high accuracy in a fully non-linear simulation.

Fields with non-trivial angular profile can be confined between the centrifugal barrier induced by the angular-momentum and the massive barrier at large distances. They can thus exhibit more colorful effects and we display the most striking one in Figs. 6, 7 and 8: the formation of a long-lived scalar cloud, resembling a “gravitational atom”, also illustrated in the animation available at [131] and the snapshots in Fig. 14.

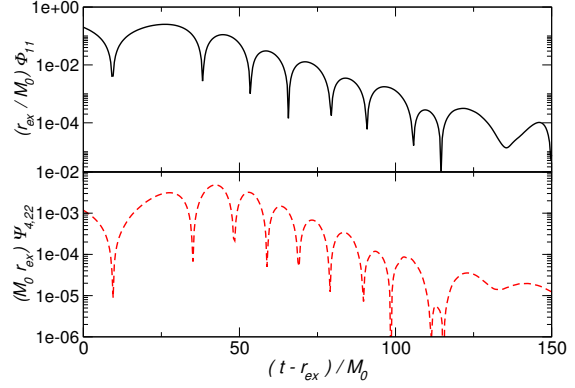
At early times, the infalling scalar field excites the BH causing an outburst of gravitational and scalar radiation. The first pulse resembles the quasinormal ringdown of a Schwarzschild BH; in fact, we find good agreement (to within 3%) between the oscillation frequencies of this early time response and those of Schwarzschild QNMs [52]. This early quasinormal ringdown stage gives way to a long-lived gravitational and scalar wave phase, as is apparent in Figs. 6 and 7.

TABLE I. Setup and initial parameters for massless scalar fields around a non-rotating BH with initial mass $M_0 = M_{\text{BH}}(0)$ and bare mass parameter $M = 1$. We denote the dimensionless location r_0/M , width w/M and amplitude MA of the scalar shell with type I or II initial profile in Sec. III A, referring, respectively, to $Z(\theta, \varphi) \sim Y_{00}$ or $Z(\theta, \varphi) \sim Y_{1-1} - Y_{11}$. Note, that we have run one simulation using *constraint violating* initial data, denoted as “CV”. We present the grid setup in the notation given by Eq. (18), where the “radii” of the refinement boxes are given in units of the bare mass x_i/M .

Run	type	r_0/M	w/M	MA	M_0	Grid setup
S00_m0_a	I	6.0	2.0	0.15	0.6859	$\{(384, 192, 96, 48, 24, 12, 6, 3, 1.5), h = M/32\}$
S00_m0_b	I	6.0	2.0	0.1	0.8626	$\{(384, 192, 96, 48, 24, 12, 6, 3, 1.5), h = M/32\}$
S00_m0_c	I	12.0	0.5	0.15	0.6858	$\{(256, 128, 64, 16, 8, 4, 2, 1), h = M/60\}$
S00_m0_d	I	12.0	0.5	0.015	0.9969	$\{(256, 128, 64, 16, 8, 4, 2, 1), h = M/60\}$
S00_m0_e	I	12.0	2.0	0.075	0.6837	$\{(256, 128, 64, 16, 8, 4, 2, 1), h = M/60\}$
S00_CV	CV	12.0	2.0	0.075	1.0	$\{(256, 128, 64, 32, 16, 8, 4, 2, 1), h = M/40\}$
S11_m0_a	II	6.0	2.0	0.04	0.7178	$\{(384, 192, 96, 48, 24, 12, 6, 3, 1.5), h = M/32\}$
S11_m0_b	II	6.0	2.0	0.03	0.8430	$\{(384, 192, 96, 48, 24, 12, 6, 3, 1.5), h = M/40\}$
S11_m0_c	II	12.0	0.5	0.03	0.6983	$\{(192, 96, 48, 24, 12, 6, 3, 1.5), h = M/60\}$
S11_m0_d	II	12.0	0.5	0.003	0.9970	$\{(192, 96, 48, 24, 12, 6, 3, 1.5), h = M/60\}$



(a) BH properties



(b) Waveforms

FIG. 4. Results for a massless scalar field around a non-rotating BH. Fig. (a) depicts the change in the BH mass (top) and the (dimensionless) angular momentum a/M_{BH} of the BH (bottom) as a function of time. The field has been set up as a shell with spherically symmetric or dipole angular configuration. Fig. (b) illustrates the $l = m = 1$ waveform (top) of the massless scalar field with an initial dipole configuration and the dominant $l = m = 2$ gravitational waveform (bottom) emitted after the accretion. Exemplarily, we present results produced by model S11_m0.c in Table I. Both waveforms, shifted in time by the extraction radius $r_{\text{ex}} = 40M$, show a clear quasi-normal ringdown signal.

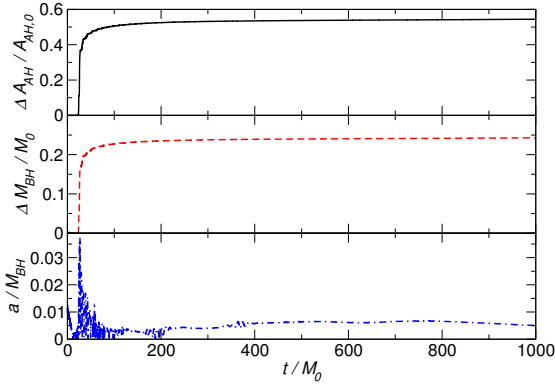
As reported recently, this long-lived state is an excitation of several closely-spaced overtones, and therefore exhibits a modulation and space-dependent excitation compatible with a beating pattern which had so far only been observed in time evolutions of scalar fields in *fixed* backgrounds [38, 58]. The long-lived scalar cloud in turn non-linearly triggers the excitation of GWs which slowly leak to infinity, explaining the long-lived states observed also in the $l = m = 2$ gravitational sector as illustrated in Fig. 7. Our results indicate that the gravitational signal is at late-times a long-lived exponentially decaying sinusoid, induced by the (long-lived) quasi-stationary scalar

field state.

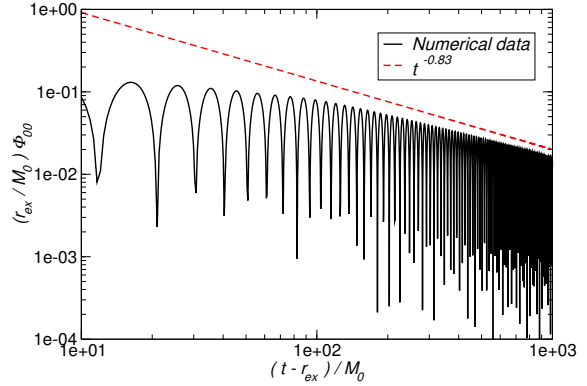
So far, we have focused only on the dominant, i.e., dipole mode. Additionally, let us inspect higher multipoles presented in Fig. 8. The waveforms exhibit beating between different modes, but also a seemingly non-linear excitation of higher multipoles. A linearized analysis shows that the beating period increases as $2l + 1$ and is of the order of our simulation timescales already for $l = 3$. Thus, it seems that the timescales probed here are not sufficient to discriminate clearly between linear and non-linear effects in the complex pattern observed in higher multipoles. The possibility that these are truly

TABLE II. Setup and initial parameters for massive scalar fields around a non-rotating BH with initial mass $M_0 = M_{\text{BH}}(0)$ and bare mass $M = 1$. We denote the initial mass coupling $M_0\mu_S$, the dimensionless location r_0/M , width w/M and amplitude MA of the scalar shell with type I or II initial profile in Sec. III A, Eqs.(27) and (31). We present the grid setup in the notation given by Eq. (18) with the “radii” of the refinement levels given in units of the bare mass M .

Run	type	$M_0\mu_S$	r_0/M	w/M	MA	M_0	Grid setup
S00_m42_a	I	0.29	6.0	2.0	0.15	0.6859	$\{(1536, 768, 384, 192, 96, 48, 24, 12, 6, 3, 1.5), h = M/32\}$
S00_m42_b	I	0.36	6.0	2.0	0.1	0.8626	$\{(1536, 768, 384, 192, 96, 48, 24, 12, 6, 3, 1.5), h = 3M/80\}$
S00_m42_c	I	0.29	12.0	0.5	0.15	0.6858	$\{(1024, 256, 128, 64, 16, 8, 4, 2, 1), h = M/60\}$
S00_m42_d	I	0.42	12.0	0.5	0.015	0.9969	$\{(1024, 256, 128, 64, 16, 8, 4, 2, 1), h = M/60\}$
S11_m42_a	II	0.30	6.0	2.0	0.04	0.7178	$\{(3072, 1536, 768, 384, 192, 96, 48, 24, 12, 6, 3, 1.5), h = M/32\}$
S11_m42_b	II	0.35	6.0	2.0	0.03	0.8430	$\{(1536, 768, 384, 192, 96, 48, 24, 12, 6, 3, 1.5), h = M/32\}$
S11_m42_c1	II	0.29	12.0	0.5	0.03	0.6983	$\{(1536, 384, 192, 32, 16, 8, 4, 2, 1), h = M/52\}$
S11_m42_c2	II	0.29	12.0	0.5	0.03	0.6983	$\{(1536, 384, 192, 32, 16, 8, 4, 2, 1), h = M/56\}$
S11_m42_c3	II	0.29	12.0	0.5	0.03	0.6983	$\{(1536, 384, 192, 32, 16, 8, 4, 2, 1), h = M/60\}$
S11_m42_d	II	0.41	12.0	0.5	0.01	0.9669	$\{(1536, 384, 192, 32, 16, 8, 4, 2, 1), h = M/60\}$
S11_m42_e	II	0.42	12.0	0.5	0.003	0.9970	$\{(1024, 256, 128, 64, 16, 8, 4, 2, 1), h = M/60\}$
S11_m77	II	0.54	12.0	0.5	0.03	0.6983	$\{(1536, 384, 192, 32, 16, 8, 4, 2, 1), h = M/60\}$



(a) BH properties



(b) waveforms and tail

FIG. 5. Evolution of a spherically symmetric massive scalar field with $M_0\mu_S = 0.29$ around a non-rotating BH. Fig. (a) depicts the relative area of the AH (top), the relative BH mass (middle) as compared to its value at $t = 0$ and the dimensionless spin parameter a/M_{BH} (bottom) as functions of time. Fig. (b) presents the $l = m = 0$ waveform of the scalar field measured at $r_{\text{ex}} = 40M$. In addition to the numerical data (black solid curve) we show a fit to the late-time tail (red dashed curve) with $t^{-0.83}$ in excellent agreement with linearized analysis.

non-linear effects akin to recently reported turbulence effects which shift the radiation to shorter scales and that might therefore lead to collapse of the field [136–139] is certainly worth exploring more in the future. It is plausible that quasi-bound (“confined”) states are also prone to such effects, but now in asymptotically flat spacetimes [122, 140].

V. RESULTS II – SCALAR CLOUDS AROUND ROTATING BHs

This section concerns the evolution of scalar fields around spinning BHs. Because this is mostly uncharted territory, we have compared our results to previous reports in the literature, by monitoring the time evolution of an isolated, highly rotating BH set up in quasi-isotropic coordinates. This analysis is done in Appendix B. Instead, the main body of the present work is devoted to the evolution of massive scalars coupled to a Kerr BH.

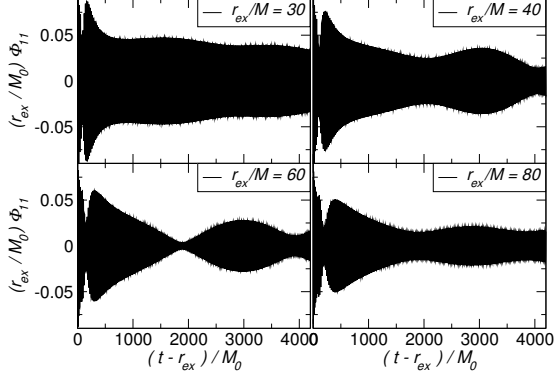


FIG. 6. $l = m = 1$ scalar field multipole for a massive, dipole scalar field with $M_0\mu_S = 0.29$ around a non-rotating BH. The waveforms, extracted at different radii r_{ex} exhibit pronounced beating patterns.

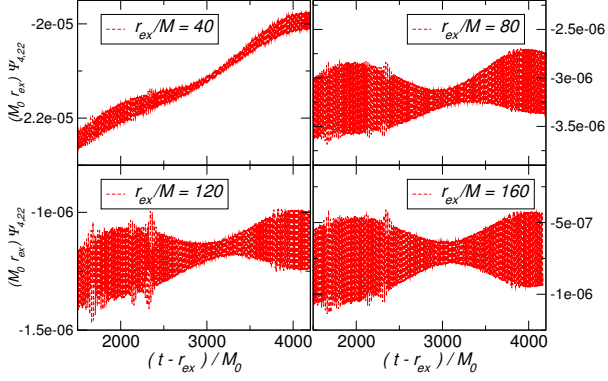


FIG. 7. $l = m = 2$ gravitational waveform for the same setup as Fig. 6.

A. Massive scalars around spinning black holes

The evolution of massive scalar fields in rotating BH spacetimes is summarized in Fig. 9, where we focus on a highly spinning BH with (initial) spin $a_0/M = 0.95$ and initial BH mass $M_0 = 1.0$. We set up the scalar shell with a dipole angular configuration either as generic Gaussian wavepacket or pseudo-bound state according to Sec. III D and Sec. III E, respectively. Unless denoted otherwise the shell has a width of $w = 2.0M$ and its maximum is centered around $r_0 = 12.0M$. In case of pseudo-bound state initial data we furthermore specify the eigenfrequency of the system which is $M\omega_B = 0.4929$ for our choice of parameters [50, 51]. Further specific parameters, such as the (initial) mass coupling $M_0\mu_S$, the amplitude A refer-

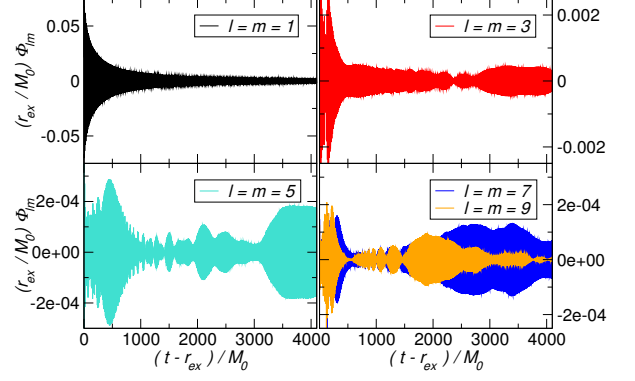


FIG. 8. We display different $l = m$ scalar multipoles, measured at $r_{\text{ex}} = 40M$, induced by a massive scalar field with initial coupling $M_0\mu_S = 0.537$. We observe, that higher multipoles are excited to a significant amount and they exhibit a colorful beating pattern.

ing to A_G or A_P for Gaussian or pseudo-bound state initial data, and the setup of the numerical domain are summarized in Table III. An animation illustrating the process is available online [131].

The time evolution has many characteristics in common with the non-rotating case discussed previously. The scalar shell is initially accreted onto the BH, and it excites the system by initiating a large burst of scalar and gravitational radiation leading to ringdown. Following this outburst of radiation a scalar cloud forms around the BH and we observe two interesting effects:

- (i) the scalar cloud is dragged along with the BH, an effect which seems to be clearly related to frame-dragging;
- (ii) the scalar cloud lightens up and dims periodically over time, like a light-house on the seashore. This is due both to the azimuthal dependence of the field as well as to the beating effects already discussed (see also Refs. [38, 58] for a thorough linear analysis).

One interesting aspect of these simulations is that they embody the properties of the initial data discussed previously: pseudo-bound state initial data shows less accretion than Gaussian initial data for comparable initial energy densities, because it was built to behave as a quasi-bound state. This property is clearly seen in Fig. 9: the GW response is similar in magnitude and has similar temporal behavior. However, the scalar field differs substantially, with much larger variations (and accretion) happening for Gaussian initial data. This property is accordingly imprinted on the gravitational-wave signal: Gaussian-type initial data induces ringdown which is followed by a power-law decay and a transition to a small, almost constant GW emission. Instead, those simulations starting with a pseudo-bound state configuration show an immediate transition to an almost constant GW

TABLE III. Setup and initial parameters for massive scalar fields around a BH with initial spin parameter $a_0/M = 0.95$ and initial BH mass $M_0 = 1$. We set up pseudo-bound state (“BS”) or Gaussian (“Ga”) type initial data described, respectively, in Sec. III E and Sec. III D. The scalar shell with width $w = 2.0M$ is located around $r_0 = 12.0M$ and has an amplitude MA . The (initial) mass coupling is given by $M_0\mu_S$. In case of pseudo-bound state initial data we employ its characteristic frequency $M\omega_B = 0.4929$. We present the grid setup in the notation given by Eq. (18), where the “radii” of the refinement levels are given in units of the bare mass parameter $M = 1$.

Run	type	$M_0\mu_S$	MA	Grid setup
AnimKerr	BS	0.35	0.075	$\{(192, 64, 32, 16, 8, 4, 2), h = M/48\}$
KBl_m35_a	BS	0.35	0.05	$\{(384, 192, 64, 32, 16, 8, 4, 2), h = M/60\}$
KBl_m35_b	BS	0.35	0.075	$\{(1536, 384, 192, 64, 32, 16, 8, 4, 2), h = M/60\}$
KGl_m30_a1	Ga	0.30	0.025	$\{(384, 192, 96, 48, 24, 12, 4, 2), h = M/52\}$
KGl_m30_a2	Ga	0.30	0.025	$\{(384, 192, 96, 48, 24, 12, 4, 2), h = M/56\}$
KGl_m30_a3	Ga	0.30	0.025	$\{(384, 192, 96, 48, 24, 12, 4, 2), h = M/60\}$
KGl_m30_b	Ga	0.30	0.075	$\{(384, 192, 96, 48, 24, 12, 4, 2), h = M/60\}$

signal in the $l = 2$ modes as shown in Fig. 9. This (almost) constant signal is powered by the continuing influx of the scalar field and thus induced stimulation of the BH. The different late-time response accommodates the fact that the generic Gaussian scalar field undergoes a transition to a pseudo-bound state, in which the scalar cloud localizes in the vicinity of the BH.

B. Hunting for superradiance

As we mentioned previously it is extremely challenging to observe scalar-field superradiance at the full non-linear level. This is due to the (relatively) short timescales over which BH systems can be evolved accurately but also due to the fact that scalar fields have a very small superradiant amplification factor of 0.04% [33]. However, we do find signs of induced *gravitational* superradiance. This claim is supported by Fig. 10, which shows the evolution of BH mass, area and spin for several initial BH spins and scalar field amplitude. These results refer to a series of simulations in which we consider a pseudo-bound state initial scalar shell centered around $r_0 = 12.0M$ with a dipole angular dependence, a width of $w = 2.0M$ and mass coupling $M_0\mu_S = 0.35$. We estimate the numerical error in the AH area, BH mass and spin to be, respectively, $\Delta A_{\text{AH}}/A_{\text{AH}} \leq 0.091\%$, $\Delta M_{\text{BH}}/M_{\text{BH}} \leq 0.0076\%$ and $\Delta a/a \leq 0.055\%$.

In the first set of runs we have fixed the scalar field amplitude to $A_P = 0.075$ and varied the initial spin of the BH in the range $a_0/M = 0, \dots, 0.95$. In the second set we have fixed the BH spin $a_0/M = 0.95$ and varied the scalar field amplitude $A_P = 0, \dots, 0.25$ and, thus, the energy content in the initial scalar cloud. The specific setups are summarized in Table IV, where we also give the critical frequency for superradiance (for the initial setup)

$$\omega_C = m\Omega_H = \frac{m}{2R_+} \left(\frac{a}{M} \right) = 2m \left(\frac{a}{M} \right) \frac{1}{M + \sqrt{M^2 - a^2}}, \quad (59)$$

in terms of the quasi-isotropic radial coordinate used in our simulations (see Eq. (46)).

A close inspection of the BH parameters reveals possibly superradiant behaviour in various time intervals at early stages of the evolution. Here, we focus on the interval $10 \leq t_1/M_0 \leq 20$.

It is apparent from Fig. 10 that for large enough initial spins both the BH mass and spin *decrease*, while the horizon area keeps increasing during this time interval. On the other hand, it is also clear that these changes are *not* dependent on the scalar field amplitude, and thus its energy density. We are thus inclined to interpret this as graviton superradiance of spurious gravitational radiation present in the initial slice. This interpretation is consistent with the superradiant amplification factors expected for spin-2 particles, whereas scalar fields have too low an amplification to explain the observed behavior [33, 52, 141, 142].

One of the main obstacles against observing scalar-field superradiance are the extremely small amplification factors for these fields. Gravitational fields on the other hand, can have amplification factors orders of magnitude larger. A recent study has shown clearly for the first time *gravitational* superradiance at the nonlinear level, by scattering of gravitational wavepackets off a spinning BH [32].

VI. CONCLUSIONS AND OUTLOOK

The physics and phenomenology of fundamental fields is extremely rich and fascinating. Current models for the evolution of the universe, dark matter and string theory all advocate the existence of light scalar degrees of freedom. Some of these ultra-light fields might have a dramatic impact on the evolution of BH systems, thus making BHs perfect laboratories to search for physics beyond the standard model. Therefore, investigating BH physics in the presence of such kind of matter is more than an academic exercise.

TABLE IV. Setup and initial parameters for massive scalar fields around a BH with initial spin parameter a_0/M and initial BH mass $M_0 = 1$. We give the corresponding critical frequency $\omega_C = m\Omega_H$ for superradiance, Eq. (1). We set up pseudo-bound states described in Sec. IIIE and specify its eigenfrequency $M\omega_B$ guided by linearized computations. The scalar shell with width $w = 2.0M$ is located around $r_0 = 12.0M$ and has an amplitude MA_P . The (initial) mass coupling is $M_0\mu_S = 0.35$. We present the grid setup in the notation given by Eq. (18), where the refinement box “radii” are given in units of the bare mass M .

Run	a_0/M	$M\omega_C$	MA_P	$M\omega_B$	Grid setup
KBs_m35_a	0.00	0.0000	0.075	0.3929	$\{(96, 48, 24, 12, 4, 2), h = M/60\}$
KBs_m35_b	0.25	0.2540	0.075	0.3929	$\{(96, 48, 24, 12, 4, 2), h = M/60\}$
KBs_m35_c	0.50	0.5359	0.075	0.3929	$\{(96, 48, 24, 12, 4, 2), h = M/60\}$
KBs_m35_d	0.90	1.2536	0.075	0.5878	$\{(96, 48, 24, 12, 4, 2), h = M/60\}$
KBs_m35_e1	0.95	1.4479	0.075	0.4929	$\{(96, 48, 24, 12, 4, 2), h = M/52\}$
KBs_m35_e2	0.95	1.4479	0.075	0.4929	$\{(96, 48, 24, 12, 4, 2), h = M/56\}$
KBs_m35_e3	0.95	1.4479	0.075	0.4929	$\{(96, 48, 24, 12, 4, 2), h = M/60\}$
KBs_m35_f	0.95	1.4479	0.000	0.4929	$\{(96, 48, 24, 12, 4, 2), h = M/60\}$
KBs_m35_g	0.95	1.4479	0.025	0.4929	$\{(96, 48, 24, 12, 4, 2), h = M/60\}$
KBs_m35_h	0.95	1.4479	0.050	0.4929	$\{(96, 48, 24, 12, 4, 2), h = M/60\}$
KBs_m35_i	0.95	1.4479	0.150	0.4929	$\{(96, 48, 24, 12, 4, 2), h = M/60\}$
KBs_m35_j	0.95	1.4479	0.250	0.4929	$\{(96, 48, 24, 12, 4, 2), h = M/60\}$

In the present paper we have started to explore the rich phenomenology of BHs encompassed by a scalar field cloud in the fully dynamical, i.e., non-linear regime of gravity. Technically, this requires to numerically evolve the coupled GR–Klein-Gordon system. One fundamental ingredient for successful numerical simulations is the construction of appropriate, *constraint-satisfying* initial configurations. We have found novel ways to prescribe initial data describing BHs surrounded by scalar clouds, either in analytic form or semi-analytically. These data provide solutions for both rotating or non-rotating BHs and (almost) monochromatic, pseudo-bound state or generic multi-frequency (Gaussian) field configurations.

These technical improvements find many interesting applications beyond the case studied in this paper. In particular, they are of utmost importance for investigations of extensions of GR which are typically motivated by string theory compactifications in the low-energy limit and involve a dilatonic or axion-like coupling. Probably the most straight-forward generalization of GR are scalar–tensor theories for which our methods apply directly.

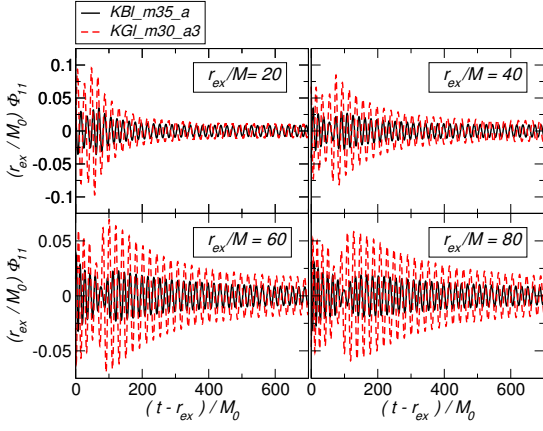
Our non-linear evolutions confirm the existence of long-lived states around BHs which slowly extract rotational energy from the BH. In previous, linearized studies this phenomenology has been used to impose stringent bounds on dark matter candidates or on the photon mass if considered as hidden U(1) vector field [49]. The fully dynamical evolutions show that the interaction of the scalar field with the central BH results in both scalar and gravitational radiation. In particular, the accretion of the scalar field triggers quasi-normal ringdown in both excitation channels. Following this first burst of radiation we witness the formation of a long-lived scalar cloud surrounding the BH which is illustrated in anima-

tions available at [131]. These (long-lived) scalar modes induce gravitational radiation with approximately twice the frequency.

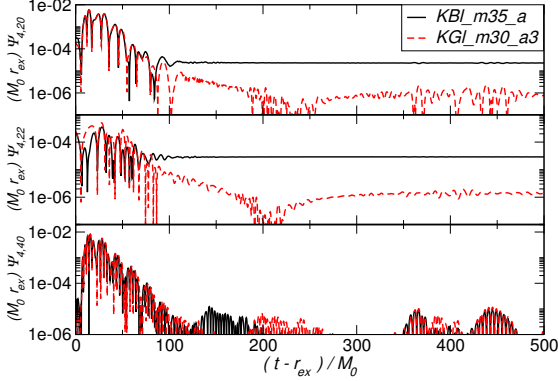
We note, that the typical frequencies emitted both in the scalar and gravitational wave channel are $f \sim \mathcal{O}(10)kHz(M/M_\odot)^{-1}$ which would potentially be observable with advLIGO or eLISA if the central BH is, respectively a solar-mass or intermediate to supermassive BH.

Furthermore, the beating pattern that we find in the scalar waveforms due to the presence of several overtone modes [38, 58] stimulates a similar behaviour of mode modulation and space dependent excitation in the gravitational channel. Additionally, in the case of a Kerr BH we directly see frame-dragging effects due to the rotation. Another exciting observation concerns the shift from an initially almost pure dipole mode towards higher multipoles. This shift hints at an energy cascade towards smaller scales which, in turn, leaves room for the exciting possibility of (gravitational) turbulent effects, similar to those found recently in asymptotically AdS spacetimes [136, 137, 139].

The present study is just a starting point to explore the rich phenomenology of BH – scalar field configurations and raise many interesting and important questions: can BHs with scalar clouds be formed during a collapse of these fundamental fields or are there other formation mechanisms at play? How would the presence of a fundamental (massive) field change the dynamics of BH binary systems? What will very long-term evolutions of these scalar clouds around BHs yield, or in other words, can we make predictions about the end-state and non-linear stability of the system? Do different multipoles interact non-linearly and eventually cascade to smaller scales, eventually collapsing and producing smaller BHs?



(a) Scalar waveforms



(b) Gravitational waveforms

FIG. 9. Waveforms for the massive scalar-cloud around a Kerr BH with $a_0/M = 0.95$. The scalar shell has been set up as pseudo-bound state (black solid curves) or Gaussian wavepacket (red dashed curves). Fig. (a) presents the $l = m = 1$ mode of the scalar field Φ_{lm} , rescaled by and presented at various extraction radii r_{ex} . Fig. (b) shows the $l = 2, m = 0$ (top), $l = m = 2$ (middle) and $l = 4, m = 0$ (bottom) modes of the gravitational waveform $\Psi_{4,lm}$ extracted at $r_{\text{ex}} = 40M$.

Other especially attractive models for future investigations – because linearized computations have shown that the superradiant instability can be tuned to be orders of magnitude larger – include mass-varying scalars and vectors, induced by coupling to matter, which arise in either scalar-tensor theories or even in the standard model [58, 61, 67, 68].

VII. ACKNOWLEDGEMENTS

We warmly thank Joan Camps, Sam Dolan, Pau Figueras and Harvey Reall as well as all the partici-

pants of the “Gravity - New perspectives from strings and higher dimensions” Benasque workshop for useful discussions and feedback. We wish to thank the anonymous referee for useful suggestions to improve the manuscript. H. O. and V. C. acknowledge financial support provided under the European Union’s FP7 ERC Starting Grant “The dynamics of black holes: testing the limits of Einstein’s theory” grant agreement no. DyBHo-256667. H. W. acknowledges financial support provided under the *ERC-2011-StG 279363-HiDGR* ERC Starting Grant and the STFC GR Roller grant ST/I002006/1. This research was supported in part by Perimeter Institute for Theoretical Physics. Research at Perimeter Institute is supported by the Government of Canada through Industry Canada and by the Province of Ontario through the Ministry of Economic Development & Innovation. This work was supported by the NRHEP 295189 FP7-PEOPLE-2011-IRSES Grant, and by FCT-Portugal through projects PTDC/FIS/116625/2010, CERN/FP/116341/2010 and CERN/FP/123593/2011. Computations were performed on the “Baltasar Sete-Sois” cluster at IST, on “venus” cluster at YITP, on the Altamira supercomputer in Cantabria through BSC grant AECT-2012-3-0012 and at the COSMOS supercomputer, part of the DiRAC HPC Facility which is funded by STFC and BIS.

Appendix A: Convergence analysis

Here we briefly discuss the numerical accuracy of our simulations. For this purpose we have evolved the dipole, massive scalar field system denoted as S11.m42_c in Table II and the initial data with angular momentum, model KGI.m30.a in Table III at three different resolutions $h_c = M/52$, $h_m = M/56$ and $h_h = M/60$, hereafter denoted as coarse, medium and high resolution runs.

The corresponding convergence plots for the scalar and gravitational radiation are presented in Figs. 11 and 12 referring, respectively, to the Schwarzschild or Kerr case. Specifically, we consider the differences between the coarse and medium and medium and high resolutions runs, where the latter difference is rescaled by the appropriate convergence factor. We present these tests exemplarily for the $l = m = 1$ mode of the scalar field Φ in Figs. 11a and 12a and the $l = m = 2$ mode of the gravitational waveform Ψ_4 , extracted at $r_{\text{ex}} = 40M$, in Figs. 11b and 12b. In both cases we find second order convergence as indicated by the factor $Q_2 = 1.24$. The convergence order is not only determined by the fourth order FD stencils but also by interpolations schemes employed, e.g. at refinement boundaries. In the present simulations it appears to dominate the numerical accuracy and, because the interpolation in time is only second order, results in an overall convergence of second order.

In the main body of this paper we have investigated both the long-term behaviour of the scalar-field – gravity system as well as the short-term behaviour which gave us

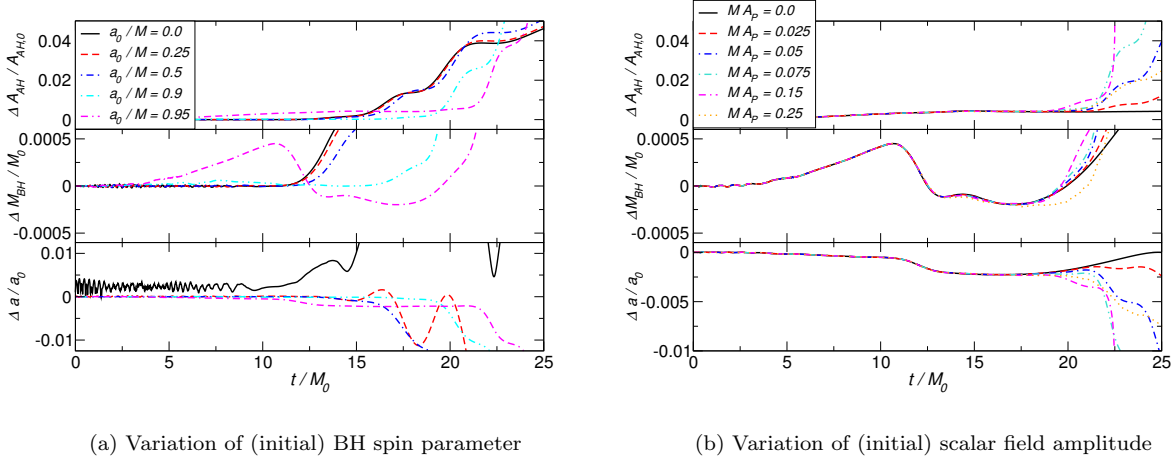


FIG. 10. We present the change in AH area (top), BH mass (middle) and BH spin (bottom) as compared to their initial values for various initial spin parameters (left) and scalar field amplitudes (right). For $a_0/M = 0.95$ we observe a decrease in both the BH mass and spin for any scalar field amplitude.

insight into the potentially superradiant regime. Therefore, we estimate the numerical error for both regimes.

Specifically, the error at early times has been measured at $t \sim 20M_0$. In this case we have focused solely on the properties of the BH and estimate the numerical error in the AH area, BH mass and spin to be, respectively, $\Delta A_{\text{AH}}/A_{\text{AH}} \leq 0.091\%$, $\Delta M_{\text{BH}}/M_{\text{BH}} \leq 0.0076\%$ and $\Delta a/a \leq 0.055\%$.

Instead, the late time numerical error which is relevant for the long-term simulations has been measured at $t \sim 3000M_0$ in the Schwarzschild and $t \sim 500M_0$ in the Kerr case. In both cases we find a numerical error of about $(8.5 \cdot 10^{-3}, 0.19, 0.16)\%$ in the AH area, BH mass and spin, respectively. The dominant scalar and gravitational waveforms exhibit a numerical error of about 6% in the Schwarzschild case and of about 2% in the Kerr case.

Additionally, we present the violation of the Hamiltonian constraint along the x-axis in Fig. 1a exemplarily for run *S00-m0-e* in Table I plotted at different instances during the evolution. We observe that initially the constraints are satisfied within less than 0.1% close to the BH horizon and better than $10^{-7}\%$ towards the outer boundary. It is important to note that the constraint violation remains small during the entire evolution; specifically they are satisfied within less than 0.1% near the BH and within less than $10^{-5}\%$ in the outer regions. The spikes that can be seen in Fig. 1a correspond to the location of the refinement boundaries.

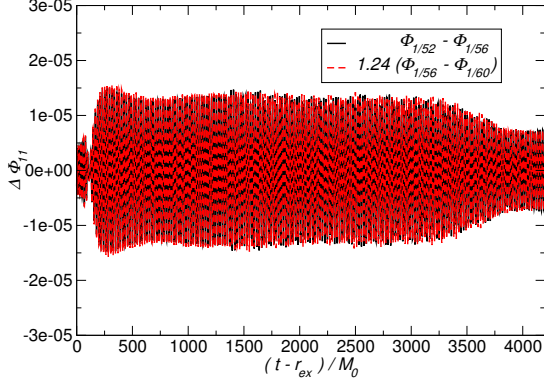
Appendix B: Benchmarking tests for a spinning BH

In order to check the performance of our code and in particular our construction of Kerr-like initial data as

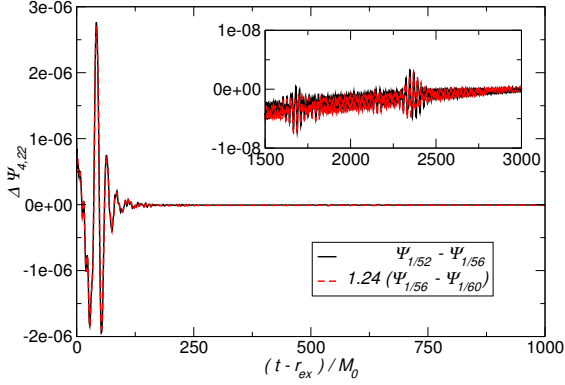
presented in Sec. III D, we have evolved a single Kerr BH without a scalar cloud. For this purpose we use a numerical domain given by $\{(192, 96, 48, 24, 16, 8, 4, 2), h = M/60\}$ in the notation of Ref. [111]. We focus on the most demanding cases that we have been able to evolve with good accuracy, namely Kerr BHs with initial spin parameters $a_0/M = 0.90$ and $a_0/M = 0.95$, where the bare mass parameter $M = 1$.

Fig. 13a shows how much the BH spin changes in time, as the system evolves freely. Until $t \sim 200M_0$ we find a decrease of $\Delta a/a_0 \lesssim 0.06\%$ (for $a_0/M = 0.90$) and $\Delta a/a_0 \lesssim 0.9\%$ (for $a_0/M = 0.95$). The bottom panel of Fig. 13b depicts the change in the BH mass which is almost constant (within $\lesssim 0.1\%$). These error estimates are comparable with the results found by Liu et al [83] (see their Fig. 1). We have furthermore verified that the AH area is indeed increasing as it should and show the time evolution of the relative AH area in the top panel of Fig. 13b.

As we have seen, the construction of conformally Kerr-like puncture initial data allows to evolve rotating BHs with spin parameters much closer to extremality than the widely used conformally flat approach which is restricted by the Bowen-York limit of $a/M \sim 0.93$ due to the presence of spurious radiation. However, even the improved, conformally Kerr-like numerical solutions contain spurious gravitational waves as we illustrate in Fig. 13c. Thus the numerical solution does not represent an isolated Kerr BH, but rather a rotating BH spacetime which also contains spurious (gravitational) radiation.



(a) Scalar field waveform

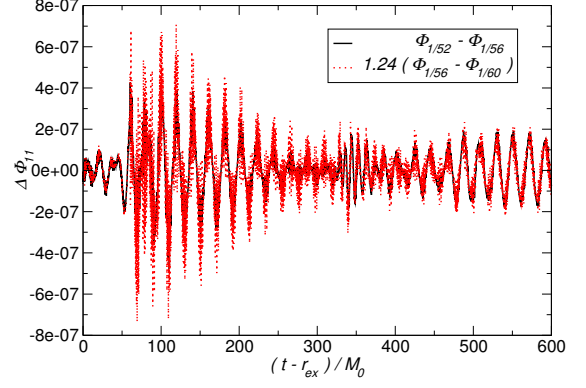


(b) Gravitational waveform

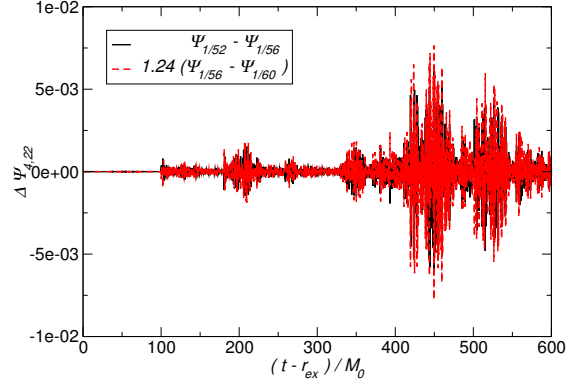
FIG. 11. Convergence plots for a massive scalar field with type II initial data and $M_0\mu_S = 0.29$ around a non-spinning BH. We present the differences in the coarse-medium and medium-high resolutions runs of the $l = m = 1$ mode of the scalar field Φ in Fig. (a) and the $l = m = 2$ mode of the gravitational waveform Ψ_4 in Fig. (b), extracted at $r_{\text{ex}} = 40M$. The latter difference has been rescaled by $Q_2 = 1.24$ indicating second order convergence. Both waveforms carry a numerical error of $< 6\%$.

Appendix C: Snapshots of scalar clouds

In order to illustrate the dynamical behaviour of a massive scalar field coupled to a BH spacetime we present snapshots of its evolutions in Figs. 14 and 15 for the case of a Schwarzschild and a Kerr BH with initial spin of $a_0/M = 0.95$. The complete animations can be found at the website [131]. Specifically we show the evolution of a dipole scalar field in the equatorial plane at different time steps. The general development is quite similar in both cases: The first plot depicts the system at early times of the evolution when the scalar field starts to be



(a) Scalar field waveform



(b) Gravitational waveform

FIG. 12. Convergence plots for runs *KGLm30_a* in Table III, i.e., for a massive scalar field with $M_0\mu_S = 0.30$ around a Kerr BH with spin parameter $a_0/M = 0.95$. We present the differences in the coarse-medium and medium-high resolutions runs of the $l = m = 1$ mode of the scalar field Φ in Fig. (a) and the $l = m = 2$ mode of the gravitational waveform Ψ_4 in Fig. (b), extracted at $r_{\text{ex}} = 40M$. The latter difference has been rescaled by $Q_2 = 1.24$ indicating second order convergence. Both waveforms carry a numerical error of $< 2\%$.

sucked into the BH. Its accretion onto the BH triggers a burst of gravitational and scalar radiation. The latter is shown in the second plot of the time series. Picture (c) and (d) of Figs. 14 and 15 illustrate the transition from the ringdown of the system towards the formation of a scalar cloud. In the second row of Figs. 14 and 15 we observe a dimming and brightening up of the massive scalar hair due to beating effects. In case of the Kerr BH, Fig. 15, the flashing of the scalar field is accompanied by a dragging of the scalar field along with the BH's rotation.

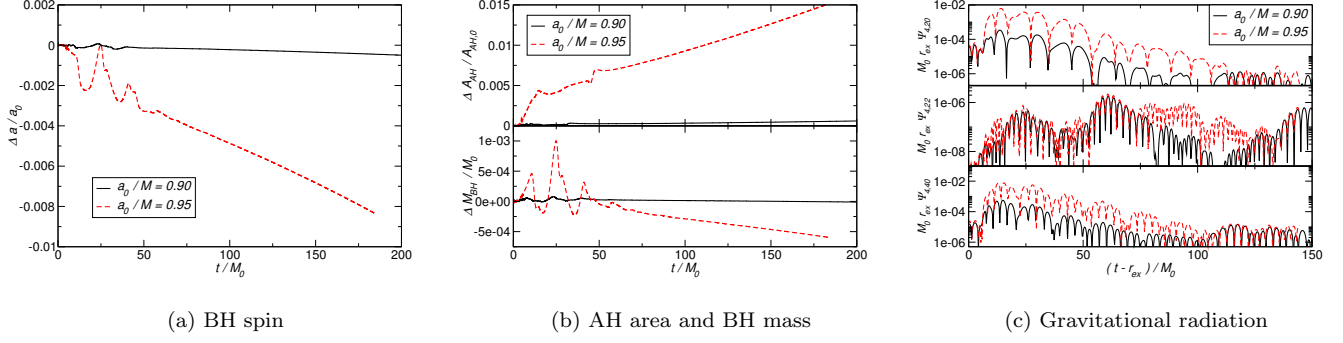


FIG. 13. Time evolution of the characteristic parameters spin (top), AH area and BH mass (middle) of a BH with initial spin $a_0/M = 0.90, 0.95$. Because the setup does not provide a pure Kerr BH gravitational radiation is present in the spacetime as illustrated by the multipoles of $\Psi_{4,lm}$ (bottom).

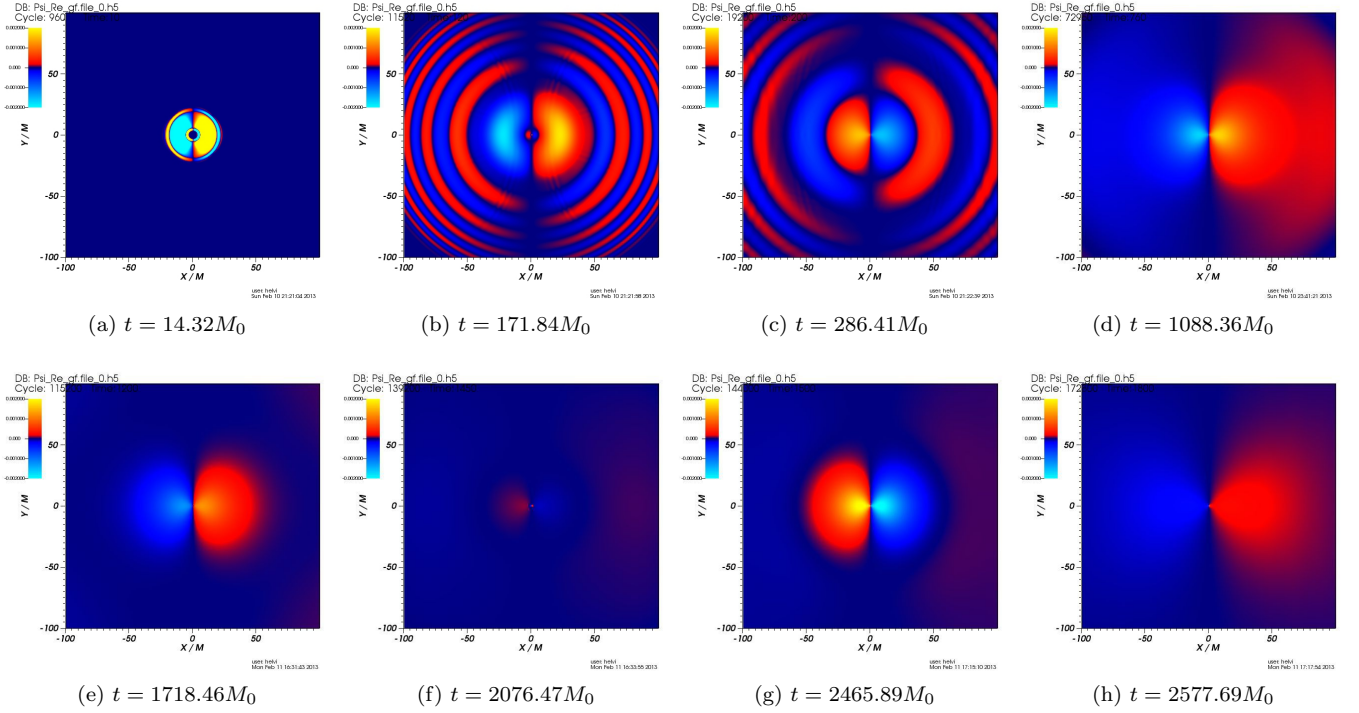


FIG. 14. Snapshots of a massive scalar cloud with $M_0 \mu_S = 0.29$ around a Schwarzschild BH with $M_0 = 0.6983$. We present a slice of the equatorial plane at different time steps. The infall of the scalar field triggers the excitation and ringdown of the BH, which is followed by the formation of a flashing scalar cloud.

-
- [1] K. Belczynski *et al.*, *Astrophys.J.* **648**, 1110 (2006), [astro-ph/0601458].
 - [2] J. E. McClintock and R. A. Remillard, 0902.3488.
 - [3] N. Ivanova *et al.*, *Astrophys.J.* **717**, 948 (2010), [1001.1767].
 - [4] S. Nissanke, M. Vallisneri, G. Nelemans and T. A. Prince, *Astrophys.J.* **758**, 131 (2012), [1201.4613].
 - [5] K. Belczynski, M. Benacquista and T. Bulik, *Astrophys.J.* **725**, 816 (2010), [0811.1602].
 - [6] C. Heinke *et al.*, *Astrophys.J.* **768**, 184 (2013), [1303.5864].
 - [7] eLISA Collaboration, P. A. Seoane *et al.*, 1305.5720.
 - [8] C. S. Reynolds, 1302.3260.

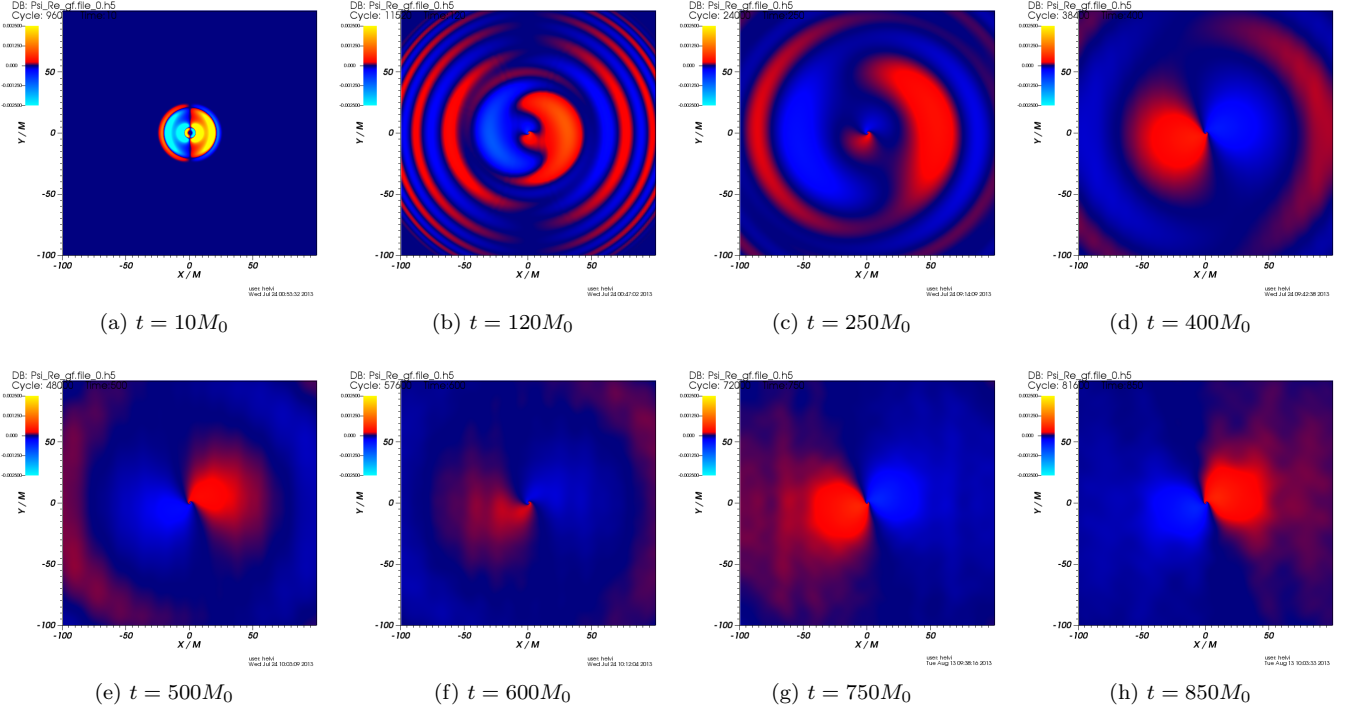


FIG. 15. Snapshots of a massive scalar cloud with $M_0\mu_S = 0.29$ around a Kerr BH with $a_0/M = 0.95$. We present a slice of the equatorial plane at different time steps. The infall of the scalar field induces a burst of gravitational and scalar waves succeeded by the formation of a flashing scalar cloud. Due to frame-dragging effects the cloud follows the rotation of the BH.

- [9] M. Begelman, R. Blandford and M. Rees, *Nature* **287**, 307 (1980).
- [10] M. J. Rees, *Ann.Rev.Astron.Astrophys.* **22**, 471 (1984).
- [11] L. Ferrarese and H. Ford, *Space Sci.Rev.* **116**, 523 (2005), [astro-ph/0411247].
- [12] T. Alexander, *Phys.Rept.* **419**, 65 (2005), [astro-ph/0508106].
- [13] L. Ferrarese *et al.*, *Astrophys.J.* **644**, L21 (2006), [astro-ph/0603840].
- [14] K. Denney *et al.*, *Astrophys.J.* **721**, 715 (2010), [1006.4160].
- [15] M. Volonteri, M. Sikora, J.-P. Lasota and A. Merloni, 1210.1025.
- [16] J. Wang, X. Zhou and J. Y. Wei, *Astrophys.J.* **768**, 176 (2013), [1303.5495].
- [17] C. S. Reynolds, 1307.3246.
- [18] LIGO Scientific Collaboration, B. Abbott *et al.*, *Rept.Prog.Phys.* **72**, 076901 (2009), [0711.3041].
- [19] F. Acernese *et al.*, *Class.Quant.Grav.* **25**, 184001 (2008).
- [20] LIGO Scientific Collaboration, Virgo Collaboration, J. Abadie *et al.*, *Phys.Rev.* **D83**, 122005 (2011), [1102.3781].
- [21] LIGO Scientific Collaboration, Virgo Collaboration, J. Aasi *et al.*, 1304.0670.
- [22] Advanced LIGO webpage, <https://www.advancedligo.mit.edu/>.
- [23] IndIGO website, <http://www.gw-indigo.org/>.
- [24] Y. Aso *et al.*, 1306.6747.
- [25] KAGRA Collaboration, K. Somiya, *Class.Quant.Grav.* **29**, 124007 (2012), [1111.7185].
- [26] P. Amaro-Seoane *et al.*, 1201.3621.
- [27] K. Eda, Y. Itoh, S. Kuroyanagi and J. Silk, *Phys.Rev.Lett.* **110**, 221101 (2013), [1301.5971].
- [28] C. F. Macedo, P. Pani, V. Cardoso and L. C. Crispino, *Astrophys.J.* **774**, 48 (2013), [1302.2646].
- [29] A. Arvanitaki and S. Dubovsky, *Phys.Rev.* **D83**, 044026 (2011), [1004.3558].
- [30] Y. B. Zel'dovich, *Pis'ma Zh. Eksp. Teor. Fiz.* **14**, 270 (1971).
- [31] Y. B. Zel'dovich, *Zh. Eksp. Teor. Fiz* **62**, 2076 (1972).
- [32] W. E. East, F. M. Ramazanoglu and F. Pretorius, 1312.4529.
- [33] W. H. Press and S. A. Teukolsky, *Nature* **238**, 211 (1972).
- [34] V. Cardoso, O. J. Dias, J. P. Lemos and S. Yoshida, *Phys.Rev.* **D70**, 044039 (2004), [hep-th/0404096].
- [35] S. Hod and O. Hod, *Phys.Rev.* **D81**, 061502 (2010), [0910.0734].
- [36] J. Rosa, *JHEP* **1006**, 015 (2010), [0912.1780].
- [37] H. Witek *et al.*, *Phys.Rev.* **D82**, 104037 (2010), [1004.4633].
- [38] S. R. Dolan, *Phys. Rev. D* **87**, 124026 (2013), [1212.1477].
- [39] R. Peccei and H. R. Quinn, *Phys.Rev.Lett.* **38**, 1440 (1977).
- [40] A. Arvanitaki, S. Dimopoulos, S. Dubovsky, N. Kaloper and J. March-Russell, *Phys.Rev.* **D81**, 123530 (2010), [0905.4720].

- [41] S. Hawking and H. Reall, Phys.Rev. **D61**, 024014 (2000), [hep-th/9908109].
- [42] V. Cardoso and O. J. Dias, Phys.Rev. **D70**, 084011 (2004), [hep-th/0405006].
- [43] V. Cardoso, O. J. Dias and S. Yoshida, Phys.Rev. **D74**, 044008 (2006), [hep-th/0607162].
- [44] V. Cardoso, O. J. C. Dias, G. S. Hartnett, L. Lehner and J. E. Santos, 1312.5323.
- [45] T. Damour, N. Deruelle and R. Ruffini, Nuovo Cimento Lettere **15**, 257 (1976).
- [46] S. L. Detweiler, Phys.Rev. **D22**, 2323 (1980).
- [47] T. Zouros and D. Eardley, Annals Phys. **118**, 139 (1979).
- [48] V. Cardoso, S. Chakrabarti, P. Pani, E. Berti and L. Gualtieri, Phys.Rev.Lett. **107**, 241101 (2011), [1109.6021].
- [49] P. Pani, V. Cardoso, L. Gualtieri, E. Berti and A. Ishibashi, Phys.Rev. **D86**, 104017 (2012), [1209.0773].
- [50] V. Cardoso and S. Yoshida, JHEP **0507**, 009 (2005), [hep-th/0502206].
- [51] S. R. Dolan, Phys.Rev. **D76**, 084001 (2007), [0705.2880].
- [52] E. Berti, V. Cardoso and A. O. Starinets, Class.Quant.Grav. **26**, 163001 (2009), [0905.2975].
- [53] J. Barranco *et al.*, Phys.Rev. **D84**, 083008 (2011), [1108.0931].
- [54] J. Barranco *et al.*, 1312.5808.
- [55] M. J. Strafuss and G. Khanna, Phys.Rev. **D71**, 024034 (2005), [gr-qc/0412023].
- [56] J. Barranco *et al.*, Phys.Rev.Lett. **109**, 081102 (2012), [1207.2153].
- [57] H. Yoshino and H. Kodama, Prog.Theor.Phys. **128**, 153 (2012), [1203.5070].
- [58] H. Witek, V. Cardoso, A. Ishibashi and U. Sperhake, Phys.Rev. **D87**, 043513 (2013), [1212.0551].
- [59] T. Damour and G. Esposito-Farese, Phys.Rev.Lett. **70**, 2220 (1993).
- [60] N. Yunes and X. Siemens, 1304.3473.
- [61] V. Cardoso, I. P. Carucci, P. Pani and T. P. Sotiriou, Phys. Rev. Lett. **111**, 111101 (2013), [1308.6587].
- [62] L. C. Stein and K. Yagi, 1310.6743.
- [63] H. Kodama and H. Yoshino, Int.J.Mod.Phys.Conf.Ser. **7**, 84 (2012), [1108.1365].
- [64] P. Pani, V. Cardoso, L. Gualtieri, E. Berti and A. Ishibashi, Phys.Rev.Lett. **109**, 131102 (2012), [1209.0465].
- [65] R. Brito, V. Cardoso and P. Pani, Phys. Rev. **D88**, 023514 (2013), [1304.6725].
- [66] R. Brito, V. Cardoso and P. Pani, Phys. Rev. **D87**, 124024 (2013), [1306.0908].
- [67] P. Pani and A. Loeb, Phys.Rev. **D88**, 041301 (2013), [1307.5176].
- [68] V. Cardoso, I. P. Carucci, P. Pani and T. P. Sotiriou, 1305.6936.
- [69] J. C. Degollado and C. A. R. Herdeiro, 1303.2392.
- [70] C. A. R. Herdeiro, J. C. Degollado and H. F. Rnarsson, 1305.5513.
- [71] J. C. Degollado and C. A. R. Herdeiro, 1312.4579.
- [72] S. Hod, Physical Review D **88**, 064055 (2013), [1310.6101].
- [73] P. Pani, E. Berti and L. Gualtieri, Phys.Rev.Lett. **110**, 241103 (2013), [1304.1160].
- [74] P. Pani, E. Berti and L. Gualtieri, 1307.7315.
- [75] J. G. Rosa and S. R. Dolan, Phys.Rev. **D85**, 044043 (2012), [1110.4494].
- [76] V. Cardoso, Gen.Rel.Grav. **45**, 2079 (2013), [1307.0038].
- [77] E. Berti, Braz.J.Phys. **43**, 341 (2013), [1302.5702].
- [78] C. A. R. Herdeiro and E. Radu, 1403.2757.
- [79] H. Yoshino and H. Kodama, 1312.2326.
- [80] G. Mocanu and D. Grumiller, Phys.Rev. **D85**, 105022 (2012), [1203.4681].
- [81] P. Pani, E. Barausse, E. Berti and V. Cardoso, Phys.Rev. **D82**, 044009 (2010), [1006.1863].
- [82] Z. Zhang, E. Berti and V. Cardoso, 1305.4306.
- [83] Y. T. Liu, Z. B. Etienne and S. L. Shapiro, Phys.Rev. **D80**, 121503 (2009), [1001.4077].
- [84] A. P. Lightman, W. H. Press, R. H. Price and S. A. Teukolsky, *Problem book in relativity and gravitation* (Princeton University Press, 1975).
- [85] R. M. Wald, (1984).
- [86] M. Alcubierre, *Introduction to 3+1 numerical relativity* (Oxford Univ. Press, Oxford, 2008).
- [87] T. W. Baumgarte and S. L. Shapiro, *Numerical Relativity* (Cambridge University Press, 2010).
- [88] J. W. York, Jr., Kinematics and dynamics of general relativity, in *Sources of Gravitational Radiation*, edited by L. L. Smarr, pp. 83–126, 1979.
- [89] E.ourgoulhon, gr-qc/0703035.
- [90] J. Centrella, J. G. Baker, B. J. Kelly and J. R. van Meter, Rev.Mod.Phys. **82**, 3069 (2010), [1010.5260].
- [91] I. Hinder, Class.Quant.Grav. **27**, 114004 (2010), [1001.5161].
- [92] T. Baumgarte and S. Shapiro, Phys.Rept. **376**, 41 (2003), [gr-qc/0211028].
- [93] R. L. Arnowitt, S. Deser and C. W. Misner, gr-qc/0405109.
- [94] O. Sarbach and M. Tiglio, Living Rev.Rel. **15**, 9 (2012), [1203.6443].
- [95] D. Hilditch, Int.J.Mod.Phys. **A28**, 1340015 (2013), [1309.2012].
- [96] T. W. Baumgarte and S. L. Shapiro, Phys.Rev. **D59**, 024007 (1999), [gr-qc/9810065].
- [97] M. Shibata and T. Nakamura, Phys.Rev. **D52**, 5428 (1995).
- [98] H. Witek, Int.J.Mod.Phys. **A28**, 1340017 (2013), [1308.1686].
- [99] M. Campanelli, C. Lousto, P. Marronetti and Y. Zlochower, Phys.Rev.Lett. **96**, 111101 (2006), [gr-qc/0511048].
- [100] J. G. Baker, J. Centrella, D.-I. Choi, M. Koppitz and J. van Meter, Phys.Rev.Lett. **96**, 111102 (2006), [gr-qc/0511103].
- [101] J. R. van Meter, J. G. Baker, M. Koppitz and D.-I. Choi, Phys.Rev. **D73**, 124011 (2006), [gr-qc/0605030].
- [102] H. Friedrich, Class. Quant. Grav. **13**, 1451 (1996).
- [103] S. A. Teukolsky, Astrophys. J. **185**, 635 (1973).
- [104] J. Thornburg, Phys.Rev. **D54**, 4899 (1996), [gr-qc/9508014].
- [105] J. Thornburg, Class.Quant.Grav. **21**, 743 (2004), [gr-qc/0306056].
- [106] D. Christodoulou, Phys.Rev.Lett. **25**, 1596 (1970).
- [107] T. Goodale *et al.*, The Cactus framework and toolkit: Design and applications, Berlin, 2003, Springer.
- [108] Cactus Computational Toolkit.
- [109] F. Löffler *et al.*, Class.Quant.Grav. **29**, 115001 (2012), [1111.3344].

- [110] Einstein Toolkit: Open software for relativistic astrophysics.
- [111] U. Sperhake, Phys.Rev. **D76**, 104015 (2007), [gr-qc/0606079].
- [112] M. Ansorg, B. Bruegmann and W. Tichy, Phys.Rev. **D70**, 064011 (2004), [gr-qc/0404056].
- [113] E. Schnetter, S. H. Hawley and I. Hawke, Class.Quant.Grav. **21**, 1465 (2004), [gr-qc/0310042].
- [114] Carpet: Adaptive Mesh Refinement for the Cactus Framework.
- [115] T. Yamamoto, M. Shibata and K. Taniguchi, Phys.Rev. **D78**, 064054 (2008), [0806.4007].
- [116] H. Okawa, International Journal of Modern Physics A (2013), [1308.3502].
- [117] M. Shibata, Phys.Rev. **D55**, 2002 (1997).
- [118] M. Shibata and K. Uryu, Phys.Rev. **D62**, 087501 (2000).
- [119] G. B. Cook, Living Rev.Rel. **3**, 5 (2000), [gr-qc/0007085].
- [120] J. Healy *et al.*, 1112.3928.
- [121] E. Berti, V. Cardoso, L. Gualtieri, M. Horbatsch and U. Sperhake, Phys.Rev. **D87**, 124020 (2013), [1304.2836].
- [122] H. Okawa, V. Cardoso and P. Pani, Phys.Rev. **D89**, 041502 (2014), [1311.1235].
- [123] D. R. Brill and R. W. Lindquist, Phys.Rev. **131**, 471 (1963).
- [124] R. W. Lindquist, J. Math. Phys. **4**, 938 (1963).
- [125] S. R. Brandt and E. Seidel, Phys.Rev. **D52**, 856 (1995), [gr-qc/9412072].
- [126] S. R. Brandt and E. Seidel, Phys.Rev. **D54**, 1403 (1996), [gr-qc/9601010].
- [127] R. Konoplya and A. Zhidenko, Phys.Rev. **D73**, 124040 (2006), [gr-qc/0605013].
- [128] R. H. Price, Phys.Rev. **D5**, 2419 (1972).
- [129] E. Ching, P. Leung, W. Suen and K. Young, Phys.Rev. **D52**, 2118 (1995), [gr-qc/9507035].
- [130] C. Gundlach, R. H. Price and J. Pullin, Phys.Rev. **D49**, 890 (1994), [gr-qc/9307010].
- [131] Gravity group CENTRA/IST Lisbon.
- [132] S. Hod and T. Piran, Phys.Rev. **D58**, 044018 (1998), [gr-qc/9801059].
- [133] H. Koyama and A. Tomimatsu, Phys.Rev. **D64**, 044014 (2001), [gr-qc/0103086].
- [134] H. Koyama and A. Tomimatsu, Phys.Rev. **D65**, 084031 (2002), [gr-qc/0112075].
- [135] L. M. Burko and G. Khanna, Phys.Rev. **D70**, 044018 (2004), [gr-qc/0403018].
- [136] P. Bizon and A. Rostworowski, Phys.Rev.Lett. **107**, 031102 (2011), [1104.3702].
- [137] M. Maliborski, Phys.Rev.Lett. **109**, 221101 (2012), [1208.2934].
- [138] A. Buchel, S. L. Liebling and L. Lehner, Phys.Rev. **D87**, 123006 (2013), [1304.4166].
- [139] A. Adams, P. M. Chesler and H. Liu, 1307.7267.
- [140] H. Yang, A. Zimmerman and L. Lehner, 1402.4859.
- [141] J. M. Bardeen, W. H. Press and S. A. Teukolsky, Astrophys.J. **178**, 347 (1972).
- [142] S. Teukolsky and W. Press, Astrophys.J. **193**, 443 (1974).